

# Noncoherent Orthogonal Time Frequency Space Modulation

Chao Xu, *Senior Member, IEEE*, Luping Xiang, *Member, IEEE*, Shinya Sugiura, *Senior Member, IEEE*, Robert G. Maunder, *Senior Member, IEEE*, Lie-Liang Yang, *Fellow, IEEE* Dusit Niyato, *Fellow, IEEE* Geoffrey Ye Li, *Fellow, IEEE* Robert Schober, *Fellow, IEEE* and Lajos Hanzo\* *Life Fellow, IEEE*

**Abstract**—The recently-developed orthogonal time frequency space (OTFS) modulation is capable of transforming the time-varying fading of the time-frequency (TF) domain into the time-invariant fading representations of the delay-Doppler (DD) domain. The OTFS system using orthogonal frequency-division multiplexing (OFDM) as inner core naturally requires the subcarrier spacing (SCS)  $\Delta f$  to be larger than the maximum Doppler frequency  $\vartheta_{\max}$ , i.e.  $\Delta f > \vartheta_{\max}$ , when perfect channel state information (CSI) knowledge is assumed. However, for the first time in literature, we explicitly demonstrate that the practical OFDM-based OTFS systems have to double their SCS in order to facilitate CSI estimation, requiring  $\Delta f' = 2\Delta f > 2\vartheta_{\max}$ . In order to mitigate this loss, we propose a novel noncoherent OTFS system, which is capable of operating at  $\Delta f > \vartheta_{\max}$ . The major challenge in this context is the mitigation of the DD-domain interference without CSI. Against this background, we draw an analogy between the input-output model of OTFS and that of V-BLAST, where V-BLAST's blind inter-antenna interference mitigation technique is invoked. Moreover, we propose to partition the DD-domain modulated symbols into groups, where space-time block coding is invoked in order to eliminate the DD-domain interference within each group. Our simulation results demonstrate that the proposed noncoherent OTFS is capable of substantially outperforming its coherent counterparts relying on CSI estimation.

**Index Terms**—Orthogonal time frequency space, delay-Doppler domain, noncoherent, channel estimation, decision-feedback, differential modulation, interference suppression, high-mobility, double-selectivity.

C. Xu, R. G. Maunder L-L. Yang and L. Hanzo are with the School of Electronics and Computer Science, University of Southampton, Southampton SO17 1BJ, UK (e-mail: {cx1g08,rm,lly,lh}@soton.ac.uk). L. Xiang is with the School of Information and Communication Engineering, University of Electronic Science and Technology of China, Chengdu 611731, China. (e-mail: luping.xiang@uestc.edu.cn). S. Sugiura is with the Institute of Industrial Science, University of Tokyo, Meguro-ku, Tokyo 153-8505, Japan (e-mail: sugiura@ieee.org). D. Niyato is with the School of Computer Science and Engineering, Nanyang Technological University, Singapore 639798 (e-mail: dniyato@ntu.edu.sg). G. Y. Li is with the Department of Electrical and Electronic Engineering, Imperial College London, London SW7 2AZ, U.K. (e-mail: geoffrey.li@imperial.ac.uk). R. Schober is with the Institute for Digital Communications, Friedrich-Alexander-Universitt Erlangen-Nrnberg(FAU), 91054 Erlangen, Germany (e-mail: robert.schober@fau.de).

The work of S. Sugiura was supported in part by the JSPS KAKENHI, Grant Number 22H01481. This research is supported by the National Research Foundation, Singapore, and Infocomm Media Development Authority under its Future Communications Research & Development Programme, DSO National Laboratories under the AI Singapore Programme (AISG Award No: AISG2-RP-2020-019 and FCP-ASTAR-TG-2022-003), and MOE Tier 1 (RG87/22). Robert Schobers work was (partly) funded by the German Ministry for Education and Research (BMBF) under the program of "Souvern. Digital. Vernetzt." joint project 6G-RIC (Project-ID 16KISK023). L. Hanzo would like to acknowledge the financial support of the Engineering and Physical Sciences Research Council projects EP/W016605/1, EP/X01228X/1 and EP/Y026721/1 as well as of the European Research Council's Advanced Fellow Grant QuantCom (Grant No. 789028).

## I. INTRODUCTION

The much-anticipated space-air-ground integrated networks (SAGIN) [1]–[4] are envisioned to be of crucial importance for next-generation systems, which will provide ubiquitous connectivity for all [5]–[7]. The International Telecommunication Union (ITU) estimates that only 63% of the world's population have Internet access [8], where the terrestrial 4G/5G networks only cover about 20% of terrestrial ground and 5% of the oceans. Moreover, billions of people are travelling in airplanes, trains and cruise ships, where the wireless access demands cannot be satisfied by the terrestrial cellular network alone. The time has come for SAGINs to support pervasive broadband services as part of the critical global infrastructure. Nonetheless, the operational cellular networks have not been designed for supporting high-mobility vehicles, such as low earth orbit (LEO) satellites, airplanes, unmanned aerial vehicles (UAVs) and high-speed trains [9]–[11]. The current 4G/5G orthogonal frequency-division multiplexing (OFDM) scheme is primarily designed for mitigating the inter-symbol interference (ISI) in time-invariant frequency-selective scenarios [12]. However, typically detrimental doubly-selective fading is encountered in high-mobility SAGIN scenarios, where the substantially increased Doppler frequency leads to inter-carrier interference (ICI) that damages OFDM's subcarrier (SC) orthogonality.

Against this background, the recently-developed orthogonal time frequency space (OTFS) modulation [13]–[15] has attracted substantial research interests as a benefit of its superior performance over OFDM in doubly-selective fading channels. More explicitly, OTFS modulates the information symbols in the two-dimensional delay-Doppler (DD) domain instead of the conventional time-frequency (TF) domain [16]–[18]. On one hand, by invoking the symplectic finite Fourier transform (SFFT), the OTFS symbols are spread over the entire TF-domain, which offers the potential of exploiting the full channel diversity [19]–[21]. On the other hand, OTFS transforms the time-varying TF-domain fading model into a time-invariant DD-domain representation of the channel parameters, including the fading gain, Doppler frequency and delay of each resolvable propagation path. As a result, the DD-domain channel state information (CSI) estimation [22], [23] no longer suffers from time-varying ISI in the time-domain (TD) or from the Doppler-induced ICI in the frequency-domain (FD), resulting in truly robust delay-/Doppler-resilience for SAGIN applications. More explicitly, some OTFS landmark papers defining the state-of-the-art are summarized in Table I along with their motivations and contributions.

TABLE I: OTFS landmark papers defining the state-of-the-art.

	Area	Motivation	Contribution
Hadani <i>et al.</i> [13]	Waveform	OFDM suffers from ICI in doubly-selective fading.	OTFS was proposed in order to facilitate a time-invariant DD-domain fading representation.
Farhang <i>et al.</i> [16]	Waveform	OTFS in [13] assumes bi-orthogonal window.	OFDM-based OTFS was conceived in order to be able to exploit existing multi-carrier infrastructure.
Raviteja <i>et al.</i> [17]	Waveform	Reducing cyclic prefix (CP) overhead.	It was demonstrated that only a single CP is needed for an OTFS frame.
RezazadehReyhani <i>et al.</i> [24]	Waveform	Enabling OTFS for MIMO.	It was proven that MIMO OFDM and MIMO OTFS have the same ergodic capacity.
Khammammetti <i>et al.</i> [25]	Waveform	Enabling OTFS for multiple access.	The DD-domain resource blocks were allocated to user terminals.
Surabhi <i>et al.</i> [19]	Diversity	Analysing the OTFS's diversity performance.	It was proven that the asymptotic diversity order of OTFS is one, but phase rotations can help OTFS to retain the full diversity gain.
Raviteja <i>et al.</i> [20]	Diversity	The worst-case PEP does not fully reflect diversity.	The effective diversity was evaluated in order to account for the majority of PEPs.
Li <i>et al.</i> [21]	Coded OTFS	Conceiving performance analysis and design guidelines for coded OTFS.	It was shown that there exists a coding-diversity gains tradeoff, where the Euclidean distance between OTFS codewords should be maximized for coded modulation.
Raviteja <i>et al.</i> [22]	CSI Estimation	Enabling joint CSI estimation and data detection.	A Dirac delta impulse signal was conceived in the DD-domain for CSI estimation, where the data symbols were also embedded in the same OTFS frame.
Shen <i>et al.</i> [23]	CSI Estimation	Reducing the dimension of CSI estimation in OTFS massive MIMO.	A 3-D orthogonal matching pursuit algorithm was proposed in order to exploit the sparsity along the spatial-/delay-/Doppler-domains.
Surabhi <i>et al.</i> [26]	Detection	Reducing the dimension of OTFS detection.	A block-circulant fading matrix structure was utilized for conceiving a low-complexity MMSE detector.
Raviteja <i>et al.</i> [27]	Detection	Mitigating the increased interference caused by fractional Doppler.	The effective MP algorithms were proposed for joint interference cancellation and symbol detection.
Yuan <i>et al.</i> [28]	Detection	Mitigating poor convergence of MP algorithms.	A variational Bayes approach was proposed, which was guaranteed to converge to the approximated MAP.
Xiang <i>et al.</i> [29]	Detection	Improving MP based on approximated MAP.	A joint MP aided detector and its low-complexity Gaussian approximated MP detector were proposed based on the exact calculation of the a posteriori probabilities.
This work	Noncoherent OTFS	Mitigating the increased SCS required for CSI estimation.	Noncoherent OTFS dispensing with CSI estimation is proposed, where blind interference suppression is conceived, and DFDD and diversity designs are invoked.

More explicitly, *first of all*, in terms of waveform design, OTFS systems have originally been constructed based on pulse-shaped OFDM (PS-OFDM) using bi-orthogonal pulses [13], [19], [27]. In order to exploit the existing multi-carrier infrastructure, OTFS waveforms based on OFDM using rectangular pulses have been advocated in [16], [17], [23], [27], where the cyclic prefix (CP) is either inserted into each OFDM symbol or into each OTFS frame. Furthermore, the incorporation of OTFS into multiple-input multiple output (MIMO) systems was proposed in [24], which proved that MIMO OFDM and MIMO OTFS have the same ergodic capacity. Moreover, OTFS-based multiple access was proposed for the uplink in [25], where the DD-domain resource blocks were allocated to user terminals. *Secondly*, in terms of the OTFS diversity performance, it was demonstrated in [19] that although the asymptotic diversity order of OTFS is one, a high diversity order is observed in the finite signal-to-noise ratio (SNR) region, and phase rotations can help OTFS to retain its full diversity gain as the SNR is increased towards infinity. Furthermore, it was argued in [20] that the strict definition of diversity order based on the worst-case pairwise error probability (PEP) does not fully characterize the OTFS diversity performance, where the effective diversity concept that characterizes the majority of PEPs was advocated. Moreover, it was shown in [21] that there exists a fundamental tradeoff between the coding gain and the diversity gain, where the Euclidean distance

between OTFS codewords should be maximized in channel-coded OTFS systems. *Thirdly*, CSI estimation operating in the DD-domain was conceived in [22], while relying on joint CSI estimation and data detection. Furthermore, CSI estimation was proposed for OTFS aided massive MIMO in [23], where a 3-D orthogonal matching pursuit algorithm was employed in order to exploit the channel's sparsity in the spatial-/delay-/Doppler-domains. *Fourthly*, one of the major challenges of OTFS is the excessive complexity of data detection, where the modulation dimension in the DD-domain is higher than that of OFDM, while OFDM's SC orthogonality can no longer be relied upon. Against this background, low-complexity minimum mean-squared error (MMSE) equalization techniques were proposed for OTFS in [26], [30]. Briefly, the block-circulant fading matrix structure was utilized in [26], while the quasi-banded structure of matrices involved in MMSE equalization was exploited in [30]. As a further advance, low-complexity linear equalization techniques were conceived for MIMO-OTFS in [31], where the doubly-circulant nature of the MIMO-OTFS channel matrix was exploited. Furthermore, by exploiting the sparsity of the DD-domain fading matrix, message passing (MP) detectors were conceived in [27]–[29], which approach the optimum maximum a posteriori (MAP) detector at a reduced complexity.

At the time of writing, noncoherent OTFS systems have not been reported, owing to the fact that CSI estimation in

the time-invariant DD-domain is considered to be of lower complexity and more accurate than CSI estimation in the time-varying TF-domain. Against this background, the following key questions arise for the noncoherent OTFS design:

- (Q-1) **Motivation:** What are the limitations of the practical coherent OTFS systems relying on CSI estimation in the DD-domain?
- (Q-2) **DD-Domain Fading:** Can noncoherent OTFS systems benefit from the time-invariant nature of the DD-domain fading channels?
- (Q-3) **DD-Domain Interference:** Can noncoherent OTFS systems mitigate the DD-domain interference without CSI?
- (Q-4) **DD-Domain Performance:** Can noncoherent OTFS systems outperform their coherent counterparts relying on practical CSI estimation?

In answer to these questions, the novel contributions of this paper are summarized as follows:

- In answer to (Q-1), we demonstrate that although the natural requirement concerning the subcarrier spacing (SCS) is that the SCS  $\Delta f$  has to be larger than the maximum Doppler frequency  $\vartheta_{\max}$ , i.e.,  $\Delta f > \vartheta_{\max}$ , the practical CSI estimation techniques of OFDM-based OTFS have to double the SCS, requiring  $\Delta f' = 2\Delta f > 2\vartheta_{\max}$ . More explicitly, the pilot embedded in OTFS transmission [22], [23], [32]–[34] aims for estimating a single column in the DD-domain channel matrix, and then the full matrix may be recovered by circular shifting, which is only valid for PS-OFDM using the idealistic bi-orthogonal pulses. By contrast, the effective channel matrices of the practical OFDM-based OTFS systems using rectangular pulses are *no longer circulant* [16], [17], [23], [27], where the fading elements in each column have specific phase rotations that are jointly determined by the row/column indices of the shifted position and the DD indices of the fading element. This requires us to double the SCS  $\Delta f' = 2\Delta f > 2\vartheta_{\max}$  in order to explicitly determine the positions and the DD indices of the non-zero fading elements in the estimated column, and then the full channel matrix can be recovered based on the estimated DD indices. Therefore, we propose the noncoherent OTFS concept for the first time in the literature, which is capable of operating at the minimum SCS of  $\Delta f > \vartheta_{\max}$  as a benefit of dispensing with CSI estimation.
- In answer to (Q-2), the noncoherent detection in the TF-domain suffers from time-varying fading channels, which lead to high-complexity noncoherent detectors that require matrix inversions for taking into account the fading correlations in the TF-domain [7], [35]–[38]. By contrast, we conceive both a recursive and a non-recursive decision-feedback differential detector (DFDD) in the DD-domain for the proposed noncoherent OTFS systems, which exhibit substantially lower complexity without any matrix inversions, thanks to the time-invariant nature of the DD-domain fading. Both phase shift keying (PSK) and quadrature amplitude modulation (QAM) are facilitated for the proposed noncoherent OTFS systems.
- As to (Q-3), we draw an analogy between the input-

output model of OTFS and that of V-BLAST, where V-BLAST's blind inter-antenna interference mitigation technique [39]–[41] is invoked for mitigating the DD-domain interference without CSI knowledge. Furthermore, we propose to partition the DD-domain modulated symbols into groups, where orthogonal space-time block coding (STBC) is invoked for eliminating the DD-domain interference within each group, leading to an improved diversity performance.

- As to (Q-4), our simulation results reveal that the proposed noncoherent OTFS schemes operating at  $\Delta f > \vartheta_{\max}$  are capable of substantially outperforming their coherent OFDM-based OTFS counterparts relying on practical CSI estimation, because the practical coherent schemes have to reduce the number of SCs and increase the modulated PSK/QAM level in order to compensate for the throughput loss due to the larger SCS of  $\Delta f' = 2\Delta f > 2\vartheta_{\max}$ .

Nonetheless, the proposed noncoherent OTFS systems also have the following limitations. Firstly, the noncoherent V-BLAST systems [39]–[41] were initially designed for transmission over a small number of antennas. As a result, the current noncoherent OTFS model designed based on noncoherent V-BLAST is more suitable for small-sized SFFT/ISFFT, which results in inevitable off-the-grid delay and Doppler shifts. Therefore, the proposed noncoherent OTFS system is constructed based on the practical assumption of fractional delays and Doppler shifts. Secondly, we note that in the absence of CSI estimation, the DD-domain MP detection<sup>1</sup> cannot be applied to noncoherent OTFS systems, owing to the fact that the positions of zeros and the values of non-zero fading elements in the sparse channel matrix are not estimated. Therefore, the DD-domain MMSE detection is applied to both the coherent and noncoherent OTFS system for a fair comparison of their achievable performance at a similar equalization complexity.

In summary, this paper is organized as follows. We demonstrate a rigorous derivation for OTFS and we devise practical CSI estimation techniques in Sec. II. The noncoherent OTFS schemes are proposed in Sec. III. Our conclusions are offered in Sec. IV.

The following notations are used throughout the paper. The operations  $(\cdot)^*$  and  $(\cdot)^H$  denote the conjugate of a complex number and the Hermitian transpose of a complex matrix, respectively. The notations  $\ln(\cdot)$  and  $\exp(\cdot)$  refer to the natural logarithm and natural exponential functions, respectively. Notations  $p(\cdot)$  and  $E(\cdot)$  represent the probability and the expectation, respectively, while  $\mathbf{a} \in \mathcal{C}^{N \times 1}$  refers to a complex-valued vector of size  $N \times 1$ , and  $\mathbf{A} \in \mathbb{C}^{c \times d}$  denotes a complex-valued matrix of size  $c \times d$ .

TABLE II: OFDM and OTFS notations.

	TD	FD	DD
Transmitter	$s_{n,m}$	$\bar{s}_{n,m}$	$\bar{s}[k,l]$
Fading	$h_{n,m,l}$	$\tilde{h}_{n,m}$	$\tilde{h}_p \omega_{MN}^{k_p(nM+m-l_p)}$
Receiver	$y_{n,m}$	$\bar{y}_{n,m}$	$\bar{y}[k,l]$

## II. COHERENT OTFS RELYING ON PRACTICAL CSI ESTIMATION

### A. General Modelling

A single antenna is used both at the transmitter and at the receiver, so that we can focus our attention on the DD-domain interference for data detection. The extension to MIMO OTFS is discussed in Sec. II-D. For the OFDM and OTFS representations, the TD, FD and DD notations follow the generic rules exemplified in Table II. An OTFS frame may also be viewed as an Inverse SFFT (ISFFT) precoding applied to  $N$  consecutive OFDM symbols, each having  $M$  subcarriers. The TD signal received under doubly-selective fading is modelled as [13]–[15]:

$$y(t) = \int \int \tilde{h}(\tau, \vartheta) s(t - \tau) e^{j2\pi\vartheta(t-\tau)} d\tau d\vartheta + v(t) \Big|_{t=\frac{nT}{M} = \frac{n}{M\Delta f}} \quad (1)$$

where  $\tau$  and  $\vartheta$  refer to the delay and Doppler frequency, while  $s(t)$  and  $v(t)$  denote the TD transmitted signal and additive white Gaussian noise (AWGN). The OFDM symbol period is  $T = \frac{1}{\Delta f}$ , where  $\Delta f$  refers to the SCS. The DD-domain fading gain in (1) is expressed as:

$$\tilde{h}(\tau, \vartheta) = \sum_{p=0}^{P-1} \tilde{h}_p \delta(\tau - \tau_p) \delta(\vartheta - \vartheta_p) \quad \begin{aligned} \tau_p &= \frac{l_p}{M\Delta f} = \frac{\check{l}_p + \delta l_p}{M\Delta f}, \\ \vartheta_p &= \frac{k_p}{NT} = \frac{\check{k}_p + \delta k_p}{NT}. \end{aligned} \quad (2)$$

On one hand, when the maximum delay exceeds the sampling period, i.e., we have  $\tau_{\max} = \max_{\forall p} \tau_p > \frac{T}{M}$ , the fading channels become frequency-selective, which imposes ISI in the TD. In frequency-selective fading channels, the total bandwidth of  $M\Delta f$  exceeds the coherence bandwidth  $B_c$ , i.e.,  $M\Delta f > B_c$  and we have  $\frac{B_c}{M} < \Delta f < B_c$ , where the FD fading is assumed to be invariant over  $\Delta f$ , but varies over  $M\Delta f$ . On the other hand, when the maximum Doppler frequency  $\vartheta_{\max} = \max_{\forall p} \vartheta_p$  becomes comparable to the SCS  $\Delta f$ , detrimental time-selectivity is encountered, which imposes ICI in the FD. This implies that the OFDM symbol period  $T$  may exceed the coherence time  $T_c$ , i.e., we have  $T > T_c > \frac{T}{M}$ , where the TD fading is assumed to be invariant over  $\frac{T}{M}$ , but varies within  $T$ . In summary, the delay and Doppler shift in (2) are sampled at  $\tau_p = \frac{l_p}{M\Delta f} = \frac{\check{l}_p + \delta l_p}{M\Delta f}$  and  $\vartheta_p = \frac{k_p}{NT} = \frac{\check{k}_p + \delta k_p}{NT}$ , where  $\check{l}_p = \lfloor l_p \rfloor$  and  $\check{k}_p = \lfloor k_p \rfloor$  denote the integer delay and Doppler indices, respectively, while  $-\frac{1}{2} < \delta l_p \leq \frac{1}{2}$  and  $-\frac{1}{2} < \delta k_p \leq \frac{1}{2}$  denote the fractional delay and Doppler indices, respectively. The ranges are given by  $0 \leq l_p < \lceil M\Delta f \tau_{\max} \rceil$  and  $-\lceil NT \vartheta_{\max} \rceil < k_p < \lceil NT \vartheta_{\max} \rceil$ . Therefore, each propagation path seen in (2) can be uniquely identified by the DD-domain parameters of fading gain  $\tilde{h}_p$ , Doppler index  $k_p = \check{k}_p + \delta k_p$  and delay index  $l_p = \check{l}_p + \delta l_p$ ,

<sup>1</sup>It has been recently reported in [42] that the TF-domain MP detection can be applied to differential schemes in a random-walk channel phase model, where the factorization of the joint probability function of the noise and channel phase is exploited. However, this cannot be applied to the OTFS regime, where the time-varying dynamics of the TF-domain fading channel are determined by the Doppler frequency instead of a random channel phase.

which are all independent of the time variable  $t$ , hence time-invariant. More explicitly, upon sampling in the TF-domain of (1) at  $t = \frac{nM+m}{M\Delta f}$  and in the DD-domain of (2) at  $(\tau_p = \frac{l_p}{M\Delta f}, \vartheta_p = \frac{k_p}{NT})$ , the relationship between the TD and DD fading representations seen in Table II can be expressed as follows:

$$h_{n,m,l} = \int \int \sum_{p=0}^{P-1} \tilde{h}_p \delta(\tau - \tau_p) \delta(\vartheta - \vartheta_p) e^{j2\pi\vartheta(t-\tau)} d\tau d\vartheta = \sum_{\forall p \in \{\check{l}_p=l\}} \tilde{h}_p \omega_{MN}^{k_p(nM+m-l_p)}, \quad (3)$$

where  $h_{n,m,l}$  models the  $l$ -th channel impulse response (CIR) tap for the  $m$ -th sample in the  $n$ -th OFDM symbol, while we have  $\omega_{MN} = \exp(j\frac{2\pi}{MN})$ . The ranges of the TF indices are given by  $0 \leq m \leq M-1$  and  $0 \leq n \leq N-1$ . Based on (3), a total number of  $P$  propagation paths associated with  $\{\tilde{h}_p\}_{p=0}^{P-1}$  and  $\{(k_p, l_p)\}_{p=0}^{P-1}$  become  $L \leq P$  CIR taps  $\{h_{n,m,l}\}_{l=0}^{L-1}$  in the TD. Naturally, some of the paths that have the same delay index  $\check{l}_p = \lfloor l_p \rfloor$  cannot be separated in the TD. They are added together in the TD by “ $\sum_{\forall p \in \{\check{l}_p=l\}}$ ” in (3). This implies that the DD-domain representation allows us to separate the propagation paths experiencing the same delay but having different Doppler frequencies. As a result, with appropriate precoding design, the OTFS family may achieve an effective diversity order of  $P \geq L$  in the DD-domain [19]–[21], which is higher than that can be achieved by the precoded OFDM in the TF-domain [43], [44].

Furthermore, for the small-scale Ricean fading assumed in this paper, the line-of-sight (LoS) path is always associated with  $l = 0$ , while the non-LoS (NLoS) paths are randomly distributed over  $0 \leq l_p < \lceil M\Delta f \tau_{\max} \rceil$ . The Doppler indices of all paths are randomly distributed over  $-\lceil NT \vartheta_{\max} \rceil < k_p < \lceil NT \vartheta_{\max} \rceil$ . The LoS and NLoS powers are determined by the Ricean  $K$  factor. The maximum Doppler frequency is given by  $\vartheta_{\max} = \frac{v f_c}{c}$ , where  $c$ ,  $f_c$  and  $v$  refer to the speed of light, carrier frequency and the vehicular speed, respectively. More explicitly, the LoS path for (3) is generated by  $h_{n,m,0} = \sqrt{\frac{K}{K+1}} \omega_{MN}^{k_0(nM+m)}$ . The NLoS paths for (3) are generated by  $\tilde{h}_p \in \mathcal{CN}(0, \frac{1}{(K+1)(P-1)})$ , i.e., complex normal distribution with mean zero and a variance of  $\frac{1}{(K+1)(P-1)}$ . As  $P$  grows large, the NLoS correlation over time follows Clarke’s model [45], [46] as  $E[h_{n,m,l} h_{n',m',l}^*] = \frac{1}{(K+1)(L-1)} J_0\left(\frac{2\pi\vartheta_{\max}[(n-n')M+(m-m')]}{M\Delta f}\right)$ , where  $J_0(\cdot)$  is the zero-th order Bessel function of the first kind.

### B. OTFS Based on Pulse-Shaped OFDM

The schematic of PS-OFDM-based OTFS [13], [19], [27] is shown in Fig. 1, which is equivalent to ISFFT-precoded PS-OFDM spanning over  $M$  SCs and  $N$  OFDM symbol durations. First of all, the OTFS transmitter modulates a total number of  $NM$  PSK/QAM symbols in the DD-domain as  $\{\{\tilde{s}[k,l]\}_{k=0}^{N-1}\}_{l=0}^{M-1}$ . The ISFFT is performed at the transmitter as follows:

$$\bar{s}[n, \bar{m}] = \frac{1}{\sqrt{NM}} \sum_{k=0}^{N-1} \sum_{l=0}^{M-1} \tilde{s}[k,l] \omega_N^{nk} \omega_M^{-\bar{m}l}. \quad (4)$$

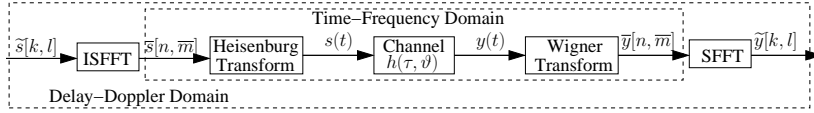


Fig. 1: Schematics of OTFS based on pulse-shaped OFDM (PS-OFDM) using bi-orthogonal pulses [13], [19], [27].

Following this, the continuous-time Heisenberg transform is invoked at the transmitter as follows:

$$s(t) = \frac{1}{\sqrt{M}} \sum_{n=0}^{N-1} \sum_{\bar{m}=0}^{M-1} \tilde{s}[n, \bar{m}] \times g_{tx}(t - nT) e^{j2\pi \bar{m} \Delta f (t - nT)} \Big|_{t = \frac{n(M+M_{cp})+m}{M} T \approx nT + \frac{m}{M} T} \quad (5)$$

where  $M_{cp}$  is the length of the CP, while  $g_{tx}(t)$  refers to the transmit PS filter. Under the condition that  $M_{cp} \ll M$ , (5) may be expressed in discrete-time as follows:

$$s[n, m] = \frac{1}{\sqrt{M}} \sum_{\bar{m}=0}^{M-1} \tilde{s}[n, \bar{m}] g_{tx}(\frac{m}{M} T) \omega_M^{\bar{m} m} = s'[n, m] g_{tx}(\frac{m}{M} T), \quad (6)$$

where we have  $s'[n, m] = \frac{1}{\sqrt{M}} \sum_{\bar{m}=0}^{M-1} \tilde{s}[n, \bar{m}] \omega_M^{\bar{m} m} = \frac{1}{\sqrt{N}} \sum_{k=0}^{N-1} \tilde{s}[k, m] \omega_N^{nk}$  based on (4). The received signal of (1) spanning over  $N$  OFDM symbol durations is expanded as follows:

$$y(t) = \int \int \sum_{p=0}^{P-1} \tilde{h}_p \delta(\tau - \tau_p) \delta(\vartheta - \vartheta_p) s(t - \tau) \times e^{j2\pi \vartheta (t - \tau)} d\tau d\vartheta + v(t) \Big|_{t = \frac{nM+m}{M} T, \tau = \frac{l}{M \Delta f}, \vartheta = \frac{k}{NT}} \quad (7)$$

which may be expressed in discrete-time form as follows:

$$y[n, m] = \sum_{l=0}^{L-1} h_{n, m, l} s[n, \langle m - l \rangle_M] + v[n, m] = \sum_{p=0}^{P-1} \tilde{h}_p \omega_{MN}^{k_p [nM+m-l_p]} s[n, \langle m - \dot{l}_p \rangle_M] + v[n, m], \quad (8)$$

where  $\langle \cdot \rangle_M$  denotes integer modulo operation of  $M$ . The OTFS receiver invokes the Wigner transform given by:

$$\bar{y}(t, f) = \int g_{rx}^*(t' - t) y(t') e^{-j2\pi f (t' - t)} dt' \Big|_{t = nT, f = \bar{m} \Delta f}, \quad (9)$$

where  $g_{rx}(t)$  refers to the receiver PS filter. The continuous-time representation of (9) may be expressed in discrete-time as (10).

Let us assume that the ideal transmitter and receiver PS filters have the following cross-ambiguity function exhibiting the bi-orthogonal property as given by (11), for  $k \in [\min_p k_p, \max_p k_p]$  and  $l \in [\min_p l_p, \max_p l_p]$ . Then the Wigner transform of (10) may be extended as (12), where we have  $y'[n, m] = \sum_{p=0}^{P-1} \tilde{h}_p \omega_{MN}^{k_p (nM-l_p)} s'[n, \langle m' - \dot{l}_p \rangle_M] + v[n, m]$ . Finally, the SFFT at the receiver leads to the input-output relationship for the OTFS waveform as given by (13), where we have  $\alpha_p(q, \delta k_p) = \frac{1}{N} \sum_{n=0}^{N-1} \omega_N^{n(q+\delta k_p)} = \frac{\omega_N^{q+\delta k_p} - 1}{N \omega_N^{q+\delta k_p} - 1}$  [22], [27]. It can be seen that for integer Doppler index associated with  $\delta k_p = 0$ , we have  $\alpha_p(q, 0) = \frac{1}{N} \sum_{n=0}^{N-1} \omega_N^{nq} = 1$ , and (13) has  $P$  non-zero DD-domain fading elements. By contrast, for fractional Doppler shift, the total number of the equivalent non-zero DD-domain fading elements in (13) is increased to  $PN$ , which introduce more interferences. Nonetheless, it was demonstrated in [22], [27] that the amplitude of  $\alpha_p(q, \delta k_p)$  peaks at  $q = 0$  and decreases rapidly as  $q$  moves away from 0. Therefore, the practical CSI estimation only needs to take into account a reduced range for  $q$ .

### C. OTFS Based on OFDM

Generating the ideal bi-orthogonal waveform of (11) is not always realistic in practice. Therefore, the OFDM-based

OTFS concept based on practical rectangular waveforms is proposed in [16], [23], [27], which is portrayed in Fig. 2. More explicitly, following the ISFFT of (4), the transmitter performs IDFT as:

$$s[n, m] = \frac{1}{\sqrt{M}} \sum_{\bar{m}=0}^{M-1} \tilde{s}[n, \bar{m}] \omega_M^{m \bar{m}} = \frac{1}{\sqrt{N}} \sum_{k=0}^{N-1} \tilde{s}[k, m] \omega_N^{nk}. \quad (14)$$

Upon obtaining the received signal of (8), the receiver performs a DFT as (15). Finally, the SFFT at the receiver leads to the input-output relationship of (16).

We note that (16) is derived under the assumptions that the CP length is small  $M_{cp} \ll M$  and a CP is inserted for each OFDM symbol for the sake of compatibility with the existing OFDM infrastructure. If a single CP is added to the entire OTFS frame, the TD circular convolution of (8) becomes MN-periodic according to:

$$y[n, m] = \sum_{p=0}^{P-1} \tilde{h}_p \omega_{MN}^{k_p [nM+m-l_p]} s[\langle nM+m-l_p \rangle_{MN}] + v[n, m], \quad (17)$$

where we have  $s[\langle nM+m-l_p \rangle_{MN}] = s[n, m - \dot{l}_p]$  for  $m \geq \dot{l}_p$  and  $s[\langle nM+m-l_p \rangle_{MN}] = s[n-1, \langle m - \dot{l}_p \rangle_M]$  for  $m < \dot{l}_p$ . As a result, the input-output relationship of (16) becomes:

$$\tilde{y}[k, l] = \sum_{p=0}^{P-1} \tilde{h}_p \sum_{q=-\frac{N}{2}}^{\frac{N}{2}-1} \tilde{T}(k, l, k_p, l_p, q) \tilde{s}[\langle k - \dot{k}_p + q \rangle_N, \langle l - \dot{l}_p \rangle_M] + \tilde{v}[k, l], \quad (18)$$

where the DD-index based phase rotations are defined as:

$$\tilde{T}(k, l, k_p, l_p, q) = \begin{cases} \omega_{MN}^{k_p (\langle l - l_p \rangle_M)} \alpha_p(q, \delta k_p), & l \geq l_p \\ \omega_N^{-k} \omega_{MN}^{k_p (\langle l - l_p \rangle_M)} \bar{\alpha}_p(q, \delta k_p), & l < l_p \end{cases}, \quad (19)$$

and we have  $\bar{\alpha}_p(q, \delta k_p) = \frac{1}{N} \sum_{n=0}^{N-1} \omega_N^{(n-1)(q+\delta k_p)}$ .

### D. OFDM and OTFS in Matrix Form

The input-output relationship of the OTFS waveforms of (13), (16) and (18) may all be expressed in the following matrix form:

$$\tilde{\mathbf{y}} = \tilde{\mathbf{H}} \tilde{\mathbf{s}} + \tilde{\mathbf{v}}. \quad (20)$$

The  $\kappa$ -th element in  $\tilde{\mathbf{y}} \in \mathcal{C}^{MN \times 1}$  is given by  $\tilde{y}_\kappa = \tilde{y}[k, l]$ , where we have  $k = \lfloor \frac{\kappa}{M} \rfloor$  and  $l = \kappa - kM$ . Similarly, the  $\kappa$ -th elements in  $\tilde{\mathbf{s}} \in \mathcal{C}^{MN \times 1}$  and  $\tilde{\mathbf{v}} \in \mathcal{C}^{MN \times 1}$  are given by  $\tilde{s}_\kappa = \tilde{s}[k, l]$  and  $\tilde{v}_\kappa = \tilde{v}[k, l]$ , respectively. The DD-domain fading matrix  $\tilde{\mathbf{H}} \in \mathcal{C}^{MN \times MN}$  is time-invariant and sparse, where the non-zero elements are given by  $\tilde{\mathbf{H}}_{\kappa, \iota} = \tilde{h}_p \omega_{MN}^{-k_p l_p} \alpha_p(q, \delta k_p)$  associated with  $\iota = M \times \langle k - \dot{k}_p + q \rangle_N + \langle l - \dot{l}_p \rangle_M$  for OTFS based on PS-OFDM of (13). Similarly, we have  $\tilde{\mathbf{H}}_{\kappa, \iota} = \tilde{h}_p \omega_{MN}^{k_p (l - l_p)} \alpha_p(q, \delta k_p)$  and  $\tilde{\mathbf{H}}_{\kappa, \iota} = \tilde{h}_p \tilde{T}(k, l, k_p, l_p, q)$  for OTFS based on OFDM using the symbol-wise CP of (16) and frame-wise CP of (18), respectively.

For a MIMO-OTFS system having  $N_t$  transmit antennas (TAs) and  $N_r$  receive antennas (RAs), the matrix form of (20) may be readily extended as from [23], [24], [47]

$$\begin{bmatrix} \tilde{\mathbf{y}}_1 \\ \tilde{\mathbf{y}}_2 \\ \vdots \\ \tilde{\mathbf{y}}_{N_r} \end{bmatrix} = \begin{bmatrix} \tilde{\mathbf{H}}_{11} & \tilde{\mathbf{H}}_{12} & \cdots & \tilde{\mathbf{H}}_{1N_t} \\ \tilde{\mathbf{H}}_{21} & \tilde{\mathbf{H}}_{22} & \cdots & \tilde{\mathbf{H}}_{2N_t} \\ \vdots & \vdots & \ddots & \vdots \\ \tilde{\mathbf{H}}_{N_r 1} & \tilde{\mathbf{H}}_{N_r 2} & \cdots & \tilde{\mathbf{H}}_{N_r N_t} \end{bmatrix} \begin{bmatrix} \tilde{\mathbf{s}}_1 \\ \tilde{\mathbf{s}}_2 \\ \vdots \\ \tilde{\mathbf{s}}_{N_t} \end{bmatrix} + \begin{bmatrix} \tilde{\mathbf{v}}_1 \\ \tilde{\mathbf{v}}_2 \\ \vdots \\ \tilde{\mathbf{v}}_{N_r} \end{bmatrix}, \quad (21)$$

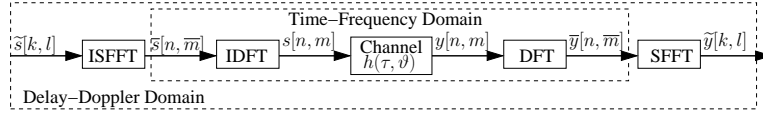


Fig. 2: Schematics of OTFS based on OFDM using rectangular pulses [16], [23], [27].

$$\begin{aligned} \bar{y}[n, \bar{m}] &= \frac{1}{\sqrt{M}} \sum_{n'=0}^{N-1} \sum_{m'=0}^{M-1} g_{rx}^* \left( (n-n')T + \frac{m'}{M}T \right) y[n', m'] \omega_M^{-\bar{m}[(n'-n)M+m']} \\ &= \frac{1}{\sqrt{M}} \sum_{n'=0}^{N-1} \sum_{m'=0}^{M-1} \sum_{p=0}^{P-1} g_{rx}^* \left( (n'-n)T + \frac{m'}{M}T \right) \tilde{h}_p s[n', < m' - \check{l}_p >_M] \omega_{MN}^{k_p[nM+m'-l_p]} \omega_M^{-\bar{m}[(n'-n)M+m']} + \bar{v}[n, \bar{m}]. \end{aligned} \quad (10)$$

$$A_{rx,tx} = \int g_{rx}^*(t' - t) g_{tx}(t') e^{-j2\pi f(t'-t)} dt' \Big|_{t=nT+\frac{m}{M}T, t'=n'T+\frac{m'}{M}T, f=\bar{m}\Delta f+\frac{k}{NT}} = \delta[n] \delta[m]. \quad (11)$$

$$\begin{aligned} \bar{y}(t, f) &= \frac{1}{\sqrt{M}} \sum_{n'=0}^{N-1} \sum_{m'=0}^{M-1} \sum_{p=0}^{P-1} g_{rx}^* \left( (n'-n)T + \frac{m'}{M}T \right) g_{tx} \left( \frac{< m' - \check{l}_p >_M T}{M} \right) \omega_{MN}^{k_p[(\bar{m}' - \bar{m})N - k_p] [(n'-n)M+m']} \\ &\quad \times \tilde{h}_p s'[n', < m' - \check{l}_p >_M] \omega_{MN}^{k_p[nM+m'-l_p]} \omega_M^{-\bar{m}[(n'-n)M+m']} + \bar{v}[n, \bar{m}] \Big|_{n=n', \bar{m}=\bar{m}'} \\ &= \frac{1}{\sqrt{M}} \sum_{m'=0}^{M-1} \sum_{p=0}^{P-1} \tilde{h}_p s'[n, < m' - \check{l}_p >_M] \omega_{MN}^{k_p(nM-m'-l_p)} \omega_M^{-\bar{m}m'} + \bar{v}[n, \bar{m}] = \frac{1}{M} \sum_{m=0}^{M-1} y'[n, m] \omega_M^{-\bar{m}m}, \end{aligned} \quad (12)$$

$$\begin{aligned} \tilde{y}[k, l] &= \frac{1}{\sqrt{MN}} \sum_{n=0}^{N-1} \sum_{\bar{m}=0}^{M-1} \bar{y}[n, \bar{m}] \omega_N^{-nk} \omega_M^{\bar{m}l} = \frac{1}{\sqrt{N}} \sum_{n=0}^{N-1} y'[n, l] \omega_N^{-nk} \\ &= \frac{1}{\sqrt{N}} \sum_{n=0}^{N-1} \sum_{p=0}^{P-1} \tilde{h}_p \omega_N^{n(k_p-k)} \omega_{MN}^{-k_p l_p} s'[n, < l - \check{l}_p >_M] + \tilde{v}[k, l] \\ &= \frac{1}{N} \sum_{n=0}^{N-1} \sum_{k'=0}^{N-1} \sum_{p=0}^{P-1} \tilde{h}_p \omega_N^{n[k'-(k-k_p)]} \omega_{MN}^{-k_p l_p} \tilde{s}[k', < l - \check{l}_p >_M] + \tilde{v}[k, l] \Big|_{k'=<k-\check{k}_p+q>N} \\ &= \sum_{p=0}^{P-1} \tilde{h}_p \omega_{MN}^{-k_p l_p} \sum_{q=-\frac{N}{2}}^{\frac{N}{2}-1} \alpha_p(q, \delta k_p) \tilde{s}[< k - \check{k}_p + q >_N, < l - \check{l}_p >_M] + \tilde{v}[k, l], \end{aligned} \quad (13)$$

$$\bar{y}[n, \bar{m}] = \frac{1}{\sqrt{M}} \sum_{m=0}^{M-1} y[n, m] \omega_M^{-m\bar{m}} = \frac{1}{\sqrt{M}} \sum_{m=0}^{M-1} \sum_{p=0}^{P-1} \tilde{h}_p s[n, < m - \check{l}_p >_M] \omega_{MN}^{k_p[nM+m-l_p]} \omega_M^{-m\bar{m}}. \quad (15)$$

$$\begin{aligned} \tilde{y}[k, l] &= \frac{1}{\sqrt{MN}} \sum_{n=0}^{N-1} \sum_{\bar{m}=0}^{M-1} \bar{y}[n, \bar{m}] \omega_N^{-nk} \omega_M^{\bar{m}l} = \frac{1}{\sqrt{N}} \sum_{n=0}^{N-1} y[n, l] \omega_N^{-nk} \\ &= \frac{1}{\sqrt{N}} \sum_{n=0}^{N-1} \sum_{p=0}^{P-1} \tilde{h}_p \omega_N^{n(k_p-k)} \omega_{MN}^{k_p(l-l_p)} s[n, < l - \check{l}_p >_M] + \tilde{v}[k, l] \\ &= \frac{1}{N} \sum_{n=0}^{N-1} \sum_{k'=0}^{N-1} \sum_{p=0}^{P-1} \tilde{h}_p \omega_N^{n[k'-(k-k_p)]} \omega_{MN}^{k_p(l-l_p)} \tilde{s}[k', < l - \check{l}_p >_M] + \tilde{v}[k, l] \Big|_{k'=<k-\check{k}_p+q>N} \\ &= \sum_{p=0}^{P-1} \tilde{h}_p \omega_{MN}^{k_p(l-l_p)} \sum_{q=-\frac{N}{2}}^{\frac{N}{2}-1} \alpha_p(q, \delta k_p) \tilde{s}[< k - \check{k}_p + q >_N, < l - \check{l}_p >_M] + \tilde{v}[k, l]. \end{aligned} \quad (16)$$

which is in the same form as the SISO model of (20). In order to avoid digressing from the main focus, the SISO model of (20) is generally assumed in this paper.

Based on (20), the DD-domain MMSE detector [26], [30] may be formulated as  $\tilde{\mathbf{z}} = (\tilde{\mathbf{H}}^H \tilde{\mathbf{H}} + N_0 \mathbf{I}_{MN})^{-1} \tilde{\mathbf{H}}^H \tilde{\mathbf{y}}$ , where  $N_0$  refers to the noise power, while  $\mathbf{I}_{MN}$  denotes identity matrix of size  $MN \times MN$ . Furthermore, based on exploiting the sparsity of  $\tilde{\mathbf{H}} \in \mathcal{C}^{MN \times MN}$ , a range of DD-domain MP detectors are conceived in [27]–[29]. Similarly, for the OFDM regime, a total number of  $NM$  PSK/QAM symbols are modulated in the TF-domain as  $\{\{\tilde{s}[n, m]\}_{n=0}^{N-1}\}_{m=0}^{M-1}$ , and the TD received signal of (8) may be expressed in matrix form for the  $n$ -th OFDM symbol as follows:

$$\mathbf{y}_n = \mathbf{H}_n \mathbf{s}_n + \mathbf{v}_n, \quad (22)$$

where the fading element on the  $r$ -th row and  $c$ -th column,  $\mathbf{H}_n(r, c) = h_{n,r,<r-c>_M}$ , is modelled based on (3). Due to the double-selectivity, the TD fading matrix  $\mathbf{H}_n$  is no longer circulant, and hence the MMSE detection may be performed in the TD as  $\mathbf{z}_n = (\mathbf{H}_n^H \mathbf{H}_n + N_0 \mathbf{I}_M)^{-1} \mathbf{H}_n^H \mathbf{y}_n$ . The MP detectors can also be conceived based on the sparsity of  $\mathbf{H}_n \in \mathcal{C}^{M \times M}$  following the same philosophy as in [27]–[29], where there are  $L$  non-zero CIR taps on each row and each column of  $\mathbf{H}_n$ . In this paper, we adopt the MMSE detection for both the OFDM and OTFS systems for the sake of fair comparison.

In order to illustrate the input-output representations, let us consider a simple OTFS system with  $N = 3$  and  $M = 3$  operating in the Ka-band at  $f_c = 38.5$  GHz and using a SCS of  $\Delta f = 30$  kHz. The vehicular speed is assumed to be 540 km/h and hence the associated maximum Doppler frequency is given by  $\vartheta_{\max} = 19.25$  kHz. The channel has  $P = 3$  resolvable paths

associated with bin-indices of  $[k_p, l_p] = \{[1, 0], [-2, 1], [2, 1]\}$ . The corresponding DD-domain fading matrices are presented in Figs. 3(a), (b) and (c), for PS-OFDM-based OTFS, for OFDM-based OTFS with symbol and frame-wise CP, respectively. Finally, the TD fading matrix of OFDM is shown in Fig. 3(d). We offer the following observations based on the input-output models of (20) and (22) as well as the examples presented in Fig. 3:

- The TD fading elements in (22) are time-varying as a function of the OFDM symbol index  $n$  and sampling index  $m$ , as exemplified by Fig. 3(d), where the phase rotations are different for each row. By contrast, the DD-domain fading matrix of (20) is intrinsically time-invariant, as exemplified by Figs. 3(a), (b) and (c).
- It is worth noting that OFDM's TD model of (22) has the advantage that the fading matrix is of lower dimension  $\mathbf{H}_n \in \mathcal{C}^{M \times M}$ , in addition to being sparse with  $L \leq P$  non-zero elements in each row and column. The disadvantage of the OFDM model is the challenge in CSI estimation in the TF-domain, i.e., time-varying frequency-selective fading.
- For the PS-OFDM-based OTFS, the DD-domain fading matrix of (20) has a favourable  $N$ -dimensional block-wise circulant structure, and each  $M \times M$ -element submatrix is also strictly circulant, as exemplified by Fig. 3(a), where the phase rotations  $\omega_9^0, \omega_9^2$  and  $\omega_9^7$  for  $\tilde{h}_0, \tilde{h}_1$  and  $\tilde{h}_2$  do not change for different positions in the matrix. Based on this beneficial feature, the CSI estimation techniques of [22], [23], [32]–[34] opt to embed a single pilot symbol in an OTFS frame in order to firstly estimate one column

$$\begin{aligned}
& \begin{bmatrix} 0 & 0 & 0 & 0 & 0 & \tilde{h}_2\omega_9^7 & \tilde{h}_0 & 0 & \tilde{h}_1\omega_9^2 \\ 0 & 0 & 0 & \tilde{h}_2\omega_9^7 & 0 & 0 & \tilde{h}_1\omega_9^2 & \tilde{h}_0 & 0 \\ 0 & 0 & 0 & 0 & \tilde{h}_2\omega_9^7 & 0 & 0 & 0 & \tilde{h}_1\omega_9^2 \\ \tilde{h}_0 & 0 & \tilde{h}_1\omega_9^2 & 0 & 0 & 0 & 0 & 0 & \tilde{h}_2\omega_9^7 \\ \tilde{h}_1\omega_9^2 & \tilde{h}_0 & 0 & 0 & 0 & 0 & \tilde{h}_2\omega_9^7 & 0 & 0 \\ 0 & \tilde{h}_1\omega_9^2 & \tilde{h}_0 & 0 & 0 & 0 & 0 & \tilde{h}_2\omega_9^7 & 0 \\ 0 & 0 & \tilde{h}_2\omega_9^7 & \tilde{h}_0 & 0 & \tilde{h}_1\omega_9^2 & 0 & 0 & 0 \\ \tilde{h}_2\omega_9^7 & 0 & 0 & \tilde{h}_1\omega_9^2 & \tilde{h}_0 & 0 & 0 & 0 & 0 \\ 0 & \tilde{h}_2\omega_9^7 & 0 & 0 & \tilde{h}_1\omega_9^2 & \tilde{h}_0 & 0 & 0 & 0 \end{bmatrix} \\
& \text{(a)} \\
& \begin{bmatrix} 0 & 0 & 0 & 0 & 0 & \tilde{h}_2\omega_9^7 & \tilde{h}_0 & 0 & \tilde{h}_1\omega_9^2 \\ 0 & 0 & 0 & \tilde{h}_2 & 0 & 0 & \tilde{h}_1 & \tilde{h}_0\omega_9 & 0 \\ 0 & 0 & 0 & 0 & \tilde{h}_2\omega_9^2 & 0 & 0 & \tilde{h}_1\omega_9^7 & \tilde{h}_0\omega_9^2 \\ \tilde{h}_0 & 0 & \tilde{h}_1\omega_9^2 & 0 & 0 & 0 & 0 & 0 & \tilde{h}_2\omega_9^7 \\ \tilde{h}_1 & \tilde{h}_0\omega_9 & 0 & 0 & 0 & 0 & \tilde{h}_2 & 0 & 0 \\ 0 & \tilde{h}_1\omega_9^7 & \tilde{h}_0\omega_9^2 & 0 & 0 & 0 & 0 & \tilde{h}_2\omega_9^7 & 0 \\ 0 & 0 & \tilde{h}_2\omega_9^7 & \tilde{h}_0 & 0 & \tilde{h}_1\omega_9^2 & 0 & 0 & 0 \\ \tilde{h}_2 & 0 & 0 & \tilde{h}_1 & \tilde{h}_0\omega_9 & 0 & 0 & 0 & 0 \\ 0 & \tilde{h}_2\omega_9^2 & 0 & 0 & \tilde{h}_1\omega_9^7 & \tilde{h}_0\omega_9^2 & 0 & 0 & 0 \end{bmatrix} \\
& \text{(b)} \\
& \begin{bmatrix} 0 & 0 & 0 & 0 & 0 & \tilde{h}_2\omega_9^4 & \tilde{h}_0 & 0 & \tilde{h}_1\omega_9^5 \\ 0 & 0 & 0 & \tilde{h}_2 & 0 & 0 & \tilde{h}_1 & \tilde{h}_0\omega_9 & 0 \\ 0 & 0 & 0 & 0 & \tilde{h}_2\omega_9^2 & 0 & 0 & \tilde{h}_1\omega_9^7 & \tilde{h}_0\omega_9^2 \\ \tilde{h}_0 & 0 & \tilde{h}_1\omega_9^2 & 0 & 0 & 0 & 0 & 0 & \tilde{h}_2\omega_9^7 \\ \tilde{h}_1 & \tilde{h}_0\omega_9 & 0 & 0 & 0 & 0 & \tilde{h}_2 & 0 & 0 \\ 0 & \tilde{h}_1\omega_9^7 & \tilde{h}_0\omega_9^2 & 0 & 0 & 0 & 0 & \tilde{h}_2\omega_9^2 & 0 \\ 0 & 0 & \tilde{h}_2\omega_9^7 & \tilde{h}_0 & 0 & \tilde{h}_1\omega_9^2 & 0 & 0 & 0 \\ \tilde{h}_2 & 0 & 0 & \tilde{h}_1 & \tilde{h}_0\omega_9 & 0 & 0 & 0 & 0 \\ 0 & \tilde{h}_2\omega_9^2 & 0 & 0 & \tilde{h}_1\omega_9^7 & \tilde{h}_0\omega_9^2 & 0 & 0 & 0 \end{bmatrix} \\
& \text{(c)} \\
& \begin{bmatrix} \tilde{h}_0\omega_9^{3n} & \tilde{h}_1\omega_9^{-2(3n-1)} + \tilde{h}_2\omega_9^{2(3n-1)} & 0 \\ 0 & \tilde{h}_0\omega_9^{3n+1} & \tilde{h}_1\omega_9^{-2(3n)} + \tilde{h}_2\omega_9^{2(3n)} \\ \tilde{h}_1\omega_9^{-2(3n+1)} + \tilde{h}_2\omega_9^{2(3n+1)} & 0 & \tilde{h}_0\omega_9^{3n+2} \end{bmatrix} \\
& \text{(d)}
\end{aligned}$$

Fig. 3: Examples of the DD-domain fading matrix of (20) and the TD fading matrix of (22), where we have  $N = 3$ ,  $M = 3$  and  $[k_p, l_p] = \{[1, 0], [-2, 1], [2, 1]\}$ . The subfigures are: (a) PS-OFDM-based OTFS; (b) OFDM-based OTFS (Symbol-wise CP); (c) OFDM-based OTFS (Frame-wise CP); (d) TD OFDM.

in the DD-domain channel matrix. Following this, the full circulant matrix can be simply recovered by circular shifting.

- For the OFDM-based OTFS using symbol/frame-wise CP, their  $M \times M$ -element submatrices are no longer circulant, as exemplified by Figs. 3(b) and (c), where the frame-wise CP case exemplified by Fig. 3(c) no longer has a block-wise circulant structure. More explicitly, the phase rotations for  $\tilde{h}_0$ ,  $\tilde{h}_1$  and  $\tilde{h}_2$  in Figs. 3(b) and (c) change from row to row. These phase rotations are jointly determined by the row/column indices of the shifted position and the DD indices of the fading element, as defined by (16) and (18). As a result, for the case of  $\vartheta_{\max} > \Delta f/2$  that may lead to  $|k_p| > \frac{N}{2}$  as exemplified by  $k_1 = -2$  and  $k_2 = 2$  in Fig. 3, the DD-domain CSI estimation method of [22] induces phase rotation ambiguities, requiring the doubling of the SCS so that all Doppler indices are unambiguously identified in  $(-\frac{N}{2}, \frac{N}{2}]$ . For example, if the Doppler index of  $k_1 = -2$  in Fig. 3 is ambiguously demodulated as  $\hat{k}_1 = k_1 + N = 1$ , the phase rotations of  $\omega_{MN}^{k_1 \langle l-l_1 \rangle M}$  defined by (16) and (18) will be evaluated wrongly. This is not an issue for the PS-OFDM-based OTFS of [22], [23], [32]–[34], where the full circulant

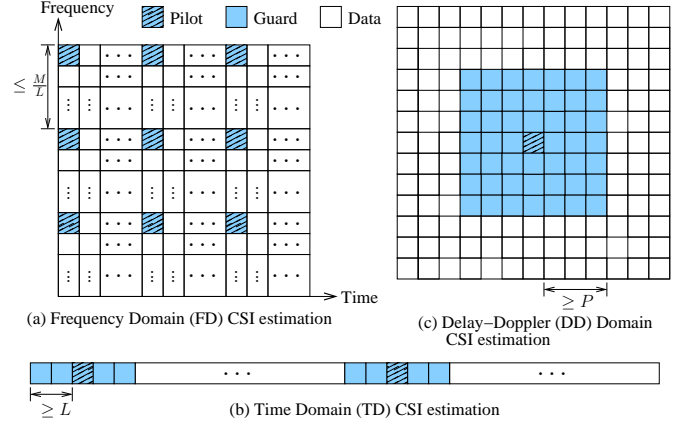


Fig. 4: Schematic illustration of FD, TD and DD-domain CSI estimation techniques.

channel matrix is recovered by circular shifting without the need of updating the phase rotations for each column.

Against this background, in the next section, we offer the revised CSI estimation schemes for the practical OFDM-based OTFS system with fractional delays and Doppler shifts.

#### E. CSI Estimation for OFDM and OTFS

A suite of FD and TD CSI estimation techniques was conceived in our previous work [2], [7], [12], [48], [49], and are illustrated in Figs. 4(a) and (b), respectively. In a nutshell, for the FD CSI estimation technique of Fig. 4(a), the pilot spacing in the FD requires  $\mathcal{N}_{PS}^{FD} \leq \frac{M}{L}$ , so that at least  $\mathcal{N}_p^{FD} = \frac{M}{\mathcal{N}_{PS}^{FD}} \geq L$  pilots are inserted at the SC indices of  $m \in \{0, \mathcal{N}_{PS}^{FD}, 2\mathcal{N}_{PS}^{FD}, \dots, (\mathcal{N}_p^{FD} - 1)\mathcal{N}_{PS}^{FD}\}$ . The first step of the FD CSI estimation technique of Fig. 4(a) follows a “horizontal comb”, where the MMSE interpolation is performed for all  $n \in \{0, \dots, N - 1\}$  associated with SC indices of  $m \in \{0, \mathcal{N}_{PS}^{FD}, 2\mathcal{N}_{PS}^{FD}, \dots, (\mathcal{N}_p^{FD} - 1)\mathcal{N}_{PS}^{FD}\}$ . Following this, “vertical comb” based pilot allocation is performed by interpolation in the FD. The FD CSI estimation technique of Fig. 4(a) operates based on the assumption of SC orthogonality, which suffers from an irreducible error floor in the face of ICI induced by double-selectivity.

Secondly, for the TD CSI estimation technique illustrated in Fig. 4(b), a Dirac delta impulse-based CSI estimation CP is inserted in the TD as:

$$s_{0,m} = \begin{cases} \rho_p^{\text{TD}}, & m = 0 \\ 0, & m = \pm 1, \pm 2, \dots, \pm \mathcal{N}_{\text{guard}}^{\text{TD}} \end{cases}, \quad (23)$$

where the power of the pilot impulse  $\rho_p^{\text{TD}} = \sum_{\forall m} |s_{0,m}|^2 = 2\mathcal{N}_{\text{cp}}^{\text{TD}} + 1$  ensures the consistency in the average transmission power over time, while the zeros in (23) define the guard intervals in Fig. 4(b). Following the TD convolution between the impulse-based pilot CP and the CIR taps, the CIRs for the CP are estimated one by one without interference, under the condition of  $\mathcal{N}_{\text{guard}}^{\text{TD}} \geq L$ . Following this, MMSE-based interpolation is performed in the TD in order to obtain the time-varying CIRs for the data symbols.

The DD-domain CSI estimation is portrayed in Fig. 4(c), where a Dirac delta impulse is transmitted in the DD-domain



based on (20) as:

$$\tilde{\mathbf{s}}_\kappa = \begin{cases} \rho_p^{\text{DD}}, & \kappa = \kappa^* \\ 0, & \kappa = \kappa_p \pm 1, \kappa_p \pm 2, \dots, \kappa_p \pm \mathcal{N}_{\text{guard}}^{\text{DD}} \\ \tilde{s}[k, l], & \text{otherwise} \end{cases}, \quad (24)$$

where the power of the pilot impulse  $\rho_p^{\text{DD}}$  can be used to maintain a constant OTFS frame power of  $MN$ . The guard interval  $\mathcal{N}_{\text{guard}}^{\text{DD}}$  is required to be larger than the number of resolvable propagation paths. We note that in contrast to the FD and TD CSI estimation techniques of [49], the DD-domain CSI estimation no longer requires MMSE based interpolation, thanks to the time-invariant DD-domain fading.

The following steps are devised for CSI estimation for the OFDM-based OTFS system with symbol-wise CP of (16), which can also be applied to the frame-wise CP of (18). First of all, any signals received within guard interval  $\tilde{\mathbf{y}}_\kappa = \tilde{y}[k, l]$  that have power higher than a threshold  $\mathcal{T}$  are considered to be obtained from the pilot symbol  $\tilde{\mathbf{x}}_{\kappa^*} = \tilde{x}[k^*, l^*]$  travelled over resolvable propagation paths, where we have  $k = \lfloor \frac{\kappa}{M} \rfloor$ ,  $l = \kappa - kM$ ,  $k^* = \lfloor \frac{\kappa^*}{M} \rfloor$  and  $l^* = \kappa^* - k^*M$  according to (20). The DD-domain fading taps have fractional Doppler and delay indices of  $\{(k_p = \ddot{k}_p + \delta k_p, l_p = \ddot{l}_p + \delta l_p)\}_{p=0}^{\hat{P}-1}$ . Based on (16), the relationships between these indices are:

$$\langle k - \ddot{k}_p + q \rangle_N = k^*, \quad \langle l - \ddot{l}_p \rangle_M = l^*. \quad (25)$$

Therefore, we can firstly detect all legitimate integer delay index as  $\hat{l}_p = \langle l - l^* \rangle_M$  for all  $|\tilde{y}[k, l]|^2 > \mathcal{T}$ . In the presence of fractional DD indices, many candidates  $|\tilde{y}[k, l]|^2 > \mathcal{T}$  share the same  $\hat{l}_p$ . The estimation on the total number of paths  $\hat{P}$  is the total number of legitimate  $\{\hat{l}_p\}_{p=0}^{\hat{P}-1}$  without repetitions. Secondly, owing to the fact that for each path  $(k_p, l_p)$ , the amplitude of  $\alpha_p(q, \delta k_p)$  peaks at  $q = 0$  [22], [27], the integer Doppler index can be demodulated as:

$$\hat{k}_p = \arg \max_{\forall k_p \in (-\lceil NT\vartheta_{\max} \rceil, \lceil NT\vartheta_{\max} \rceil]} |\tilde{y}[\langle k^* + \ddot{k}_p \rangle_N, \langle l^* + \hat{l}_p \rangle_M]|^2, \quad (26)$$

for  $p = 0, 1, \dots, \hat{P} - 1$ . Thirdly, according to (16), the fading elements associated with the same path  $(k_p, l_p)$  only differ in  $\alpha_p(q, \delta k_p)$ . Therefore, the fractional Doppler index can be demodulated with a pre-defined precision within  $\delta k_p \in (-\frac{1}{2}, \frac{1}{2}]$  as:

$$\delta \hat{k}_p = \arg \min_{\delta k_p \in (-\frac{1}{2}, \frac{1}{2}]} \left| \frac{\tilde{y}[\langle k^* + \hat{k}_p \rangle_N, \langle l^* + \hat{l}_p \rangle_M]}{\tilde{y}[\langle k^* + \hat{k}_p - 1 \rangle_N, \langle l^* + \hat{l}_p \rangle_M]} - \frac{\alpha_p(0, \delta k_p)}{\alpha_p(1, \delta k_p)} \right|, \quad (27)$$

for  $p = 0, 1, \dots, \hat{P} - 1$ . As a result, the complete Doppler indices are give by  $\{\hat{k}_p = \hat{k}_p + \delta \hat{k}_p\}_{p=0}^{\hat{P}-1}$ . Following this, the fading element is estimated by:

$$\tilde{h}_p = \frac{\tilde{y}[k, l]}{\rho_p^{\text{DD}} \omega_{MN}^{\hat{k}_p(l - \hat{l}_p)} \alpha_p(0, \delta \hat{k}_p)} \Big|_{k = \langle k^* + \hat{k}_p \rangle_N, l = \langle l^* + \hat{l}_p \rangle_M}, \quad (28)$$

for  $p = 0, 1, \dots, \hat{P} - 1$ . Finally, the estimation on the channel matrix is fully constructed based on (16) as:

$$\tilde{\mathbf{H}}_{\kappa, \iota} = \tilde{h}_p \omega_{MN}^{\hat{k}_p(l - \hat{l}_p)} \alpha_p(q, \delta \hat{k}_p), \quad (29)$$

for all  $k \in [0, N - 1]$ ,  $l \in [0, M - 1]$ ,  $p \in [0, \hat{P} - 1]$  and  $q \in [-\frac{N}{2}, \frac{N}{2} - 1]$ , where we have  $\kappa = kM + l$  and  $\iota =$


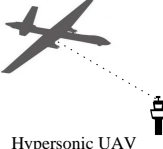
		
Distance	10~20 km	>200 nautical miles
Ricean K	$K = -3$ dB	$K = 3$ dB
Speed	540 km/h	Mach 7
$f_c$	38.5 GHz (K-band)	2.6 GHz (S-band)
$\vartheta_{\max}$	19.25 kHz	20.75 kHz
$\Delta f$	30 kHz, 60 kHz	

Fig. 5: Scenarios and parameters considered in this paper.

$M < k - \hat{k}_p + q >_N + \langle l - \hat{l}_p \rangle_M$ . We note that there is no need to estimate the fractional delay index  $\delta l_p$ , because the phase rotation of  $\omega_{MN}^{-\hat{k}_p \delta l_p}$  is shared by all fading elements and is included in  $\tilde{h}_p$ , i.e. we have  $\tilde{h}_p = \tilde{h}_p \omega_{MN}^{-\hat{k}_p \delta l_p}$  and then  $\tilde{h}_p \omega_{MN}^{\hat{k}_p(l - \hat{l}_p)} = \tilde{h}_p \omega_{MN}^{\hat{k}_p(l - \hat{l}_p)}$  for all fading elements, where  $\hat{l}_p = \hat{l}_p + \delta l_p$ .

Let us once again shed some light on the issue of SCS. When we have  $\frac{\Delta f}{2} < \vartheta_{\max} < \Delta f$ , a negative  $\ddot{k}_p$  and its positive counterpart  $\ddot{k}_p + N$  are both within the legitimate range of  $(-\lceil N \frac{\vartheta_{\max}}{\Delta f} \rceil, \lceil N \frac{\vartheta_{\max}}{\Delta f} \rceil)$ . Therefore, both  $\ddot{k}_p$  and  $\ddot{k}_p + N$  lead to the same location index  $\langle k^* + \ddot{k}_p \rangle_N$  in (26) but different phase rotation values for  $\omega_{MN}^{\ddot{k}_p(l - \hat{l}_p)}$  in (28), which leads to severe error in recovering the full channel matrix in (29). Therefore, the SCS has to be doubled to  $\Delta f' = 2\Delta f$ , so that the reduced range of  $(-\lceil N \frac{\vartheta_{\max}}{2\Delta f} \rceil, \lceil N \frac{\vartheta_{\max}}{2\Delta f} \rceil)$  will only contain a single legitimate candidate for  $\ddot{k}_p$ . Once again, this is not an issue for the PS-OFDM-based OTFS of [22], [23], [32]–[34], where the full circulant channel matrix is recovered by circular shifting without the need for updating the phase rotations for each column.

In summary, the CSI estimation algorithm for the OFDM-based OTFS system with symbol-wise CP is summarized in Table III. We note that this algorithm can be directly applied to frame-wise CP of (18), when the pilot position is set to be  $\kappa^* = k^* = l^* = 0$ , which is also the preferred simple choice for symbol-wise CP. The only modification required is that the channel matrix construction of (29) should be replaced by the following equation based on (18):

$$\tilde{\mathbf{H}}_{\kappa, \iota} = \tilde{h}_p \tilde{T}(k, l, \hat{k}_p, \hat{l}_p, q). \quad (30)$$

#### F. Simulation Results for CSI Estimation

First of all, the scenarios and simulation parameters considered in this paper are summarized in Fig. 5. More explicitly, the high-speed trains are expected to reach an average speed of over 500 km/h, and the coverage is expected to be up to 20 km [11], [50]–[53]. The railway cuttings, the curved routes and the high operating frequency of the millimeter-wave band often lead to reduced LoS power [11], [51], [52]. Against this background, we assume a train speed of 540 km/h and an operating frequency of 38.5 GHz in the 5G millimeter-wave band, leading to the maximum Doppler frequency of  $\vartheta_{\max} = 19.25$  kHz as shown in Fig. 5. For airplanes, typically lower frequency bands are used for long-range aeronautical communications, where the coverage may reach over 200 nautical miles [2], [3], [54], [55]. Due to the altitude of the airplane, often a LoS is observed [56], but the



TABLE III: Summary of CSI estimation for the OFDM-based OTFS system with symbol-wise CP.

<b>Input:</b> $\tilde{\mathbf{y}}, \tilde{\mathbf{s}}_{\kappa^*} = \rho_p^{\text{DD}}, \mathcal{N}_{\text{guard}}^{\text{DD}}, \mathcal{T}$ .	<b>Output:</b> $\tilde{\mathbf{H}}$ .
<b>Relationships between indices:</b> $k = \lfloor \frac{\kappa^*}{M} \rfloor$ , $l = \kappa - kM$ , $k^* = \lfloor \frac{\kappa^*}{M} \rfloor$ , $l^* = \kappa^* - k^*M$ , $k_p = \hat{k}_p + \delta k_p$ , $l_p = \hat{l}_p + \delta l_p$ , $\langle k - \hat{k}_p + q \rangle_N = k^*$ , $\langle l - \hat{l}_p \rangle_M = l^*$ .	
<b>Step 1 (Integer delay indice and number of paths):</b> For all $ \tilde{y}[k, l] ^2 > \mathcal{T}$ within guard internal, the integer delay indice are demodulated as $\hat{l}_p = \langle l - l^* \rangle_M$ . The estimated number of paths $\hat{P}$ is the number of legitimate $\{\hat{l}_p\}_{p=0}^{\hat{P}-1}$ without repetitions.	
<b>Step 2 (Integer Doppler indices):</b> $\hat{k}_p = \arg \max_{\hat{k}_p \in (-\lceil NT\vartheta_{\max} \rceil, \lceil NT\vartheta_{\max} \rceil]}  \tilde{y}[\langle k^* + \hat{k}_p \rangle_N, \langle l^* + \hat{l}_p \rangle_M] ^2$ .	
<b>Step 3 (Fractional Doppler indices):</b> $\delta \hat{k}_p = \arg \min_{\delta k_p \in (-\frac{1}{2}, \frac{1}{2})} \left  \frac{\tilde{y}[\langle k^* + \hat{k}_p \rangle_N, \langle l^* + \hat{l}_p \rangle_M]}{\tilde{y}[\langle k^* + \hat{k}_p - 1 \rangle_N, \langle l^* + \hat{l}_p \rangle_M]} - \frac{\alpha_p(0, \delta k_p)}{\alpha_p(1, \delta k_p)} \right ^2$ for $p = 0, 1, \dots, \hat{P} - 1$ .	
Therefore, the complete Doppler indices are give by $\{\hat{k}_p = \hat{k}_p + \delta \hat{k}_p\}_{p=0}^{\hat{P}-1}$ .	
<b>Step 4 (Fading elements):</b> $\tilde{h}_p = \frac{\tilde{y}[k, l]}{\rho_p^{\text{DD}} \omega_{MN}^{\hat{k}_p(l - \hat{l}_p)} \alpha_p(0, \delta \hat{k}_p)}$ using $k = \langle k^* + \hat{k}_p \rangle_N$ and $l = \langle l^* + \hat{l}_p \rangle_M$ for $p = 0, 1, \dots, \hat{P} - 1$ .	
<b>Step 5 (Fading matrix):</b> $\tilde{\mathbf{H}}_{\kappa, \iota} = \tilde{h}_p \omega_{MN}^{\hat{k}_p(l - \hat{l}_p)} \alpha_p(q, \delta \hat{k}_p)$ , for all $k \in [0, N - 1]$ , $l \in [0, M - 1]$ , $p \in [0, \hat{P} - 1]$ and $q \in [-\frac{N}{2}, \frac{N}{2} - 1]$ , where we have $\kappa = kM + l$ and $\iota = M \langle k - \hat{k}_p + q \rangle_N + \langle l - \hat{l}_p \rangle_M$ .	

airframe shadowing effect due to aircraft maneuvering may substantially reduce the Ricean K factor [2], [3], [54], [57]. In Fig. 5, we consider a hypersonic UAV scenario, where the vehicular speed is Mach 7 and the operating frequency is 2.6 GHz, which results in a maximum Doppler frequency of  $\vartheta_{\max} = 20.75$  kHz. The SCS  $\Delta f = \{30, 60\}$  kHz used in 5G scalable numerology [58] are invoked. Interested readers may refer to [1]–[4] for more details on SAGIN scenarios and parameters. Moreover, we note that the fractional delays and Doppler shifts are randomly generated between  $[0, \tau_{\max}]$  and  $[-\vartheta_{\max}, \vartheta_{\max}]$ , respectively. The precision for fractional Doppler detection of (27) is set to be 0.1.

Fig. 6 portrays the effect of SCS  $\Delta f$  on the DD-domain CSI estimation. The power of the DD-domain pilot  $P_t^{\text{pilot}}$  is adjusted with respect to the average OTFS frame power  $P_t^{\text{OTFS}}$  in order to balance the pilot-data transmission pattern. Fig. 6(a) confirms that the PS-OFDM-based OTFS system relying on the idealistic bi-orthogonal pulse is capable of performing effective CSI estimation without having to increase the SCS, even when we have  $\vartheta_{\max} > \frac{\Delta f}{2}$ . By contrast, Figs. 6(b) and (c) demonstrate that the OFDM-based OTFS systems relying on rectangular pulses suffer from irreducible error floors, when the DD-domain CSI estimation is performed at  $\Delta f = 30$  kHz, regardless of the pilot power. As a remedy, the SCS has to be doubled to  $\Delta f' = 60$  kHz in order to facilitate the DD-domain CSI estimation in Figs. 6(b) and (c), where  $M$  is halved and QPSK is replaced by 16QAM in order to convey the same throughput given the same system bandwidth. Observe in Figs. 6(b) and (c) that the CSI estimation methods for OFDM-based OTFS devised in Sec. II-E are capable of both approaching to the case of perfect CSI at  $\Delta f' = 60$  kHz and outperforming OFDM. However, the OFDM-based OTFS systems operating at  $\Delta f' = 60$  kHz suffer from significant performance loss compared to the ideal case of perfect CSI at  $\Delta f = 30$  kHz.

The BER performance results of Fig. 6 are further confirmed by the discrete-input continuous-output memoryless channel (DCMC) capacity results of Fig. 7. More explicitly, the DCMC capacity [59]–[61] is evaluated based on (31), where the mutual information is maximized, when the modulated  $\mathcal{L}$ -PSK/QAM symbols are equiprobable, i.e., we have  $\{p(\tilde{\mathbf{s}}_{\kappa} = \tilde{s}^i)\} = \frac{1}{\mathcal{L}} \}_{i=1}^{\mathcal{L}}$ . For coherent OTFS based on MMSE detection,

the conditional probability is given by:

$$p(\tilde{\mathbf{z}}_{\kappa} | \tilde{s}^i) = \frac{1}{\pi \tilde{N}_{0, \kappa}} \exp\left(-\frac{|\tilde{\mathbf{z}}_{\kappa} - \tilde{s}^i|^2}{\tilde{N}_{0, \kappa}}\right), \quad (32)$$

where  $\tilde{\mathbf{z}}_{\kappa}$  is the  $\kappa$ -th element in  $\tilde{\mathbf{z}} = \tilde{\mathbf{G}}_{\text{MMSE}} \tilde{\mathbf{y}}$  using  $\tilde{\mathbf{G}}_{\text{MMSE}} = (\tilde{\mathbf{H}}^H \tilde{\mathbf{H}} + N_0 \mathbf{I}_{MN})^{-1} \tilde{\mathbf{H}}^H$  based on (20), while  $\tilde{N}_{0, \kappa}$  is the  $\kappa$ -th diagonal element in  $N_0 \tilde{\mathbf{G}}_{\text{MMSE}} \tilde{\mathbf{G}}_{\text{MMSE}}^H$ .

The DCMC capacity results of Fig. 7(a) confirm the BER result of Fig. 6(a) that the PS-OFDM-based OTFS system is capable of performing effective CSI estimation at  $\Delta f = 30$  kHz for the UAV scenario in Fig. 5, when the maximum Doppler frequency is  $\vartheta_{\max} = 20.75$  kHz. Furthermore, Fig. 7(b) and (c) demonstrate that the CSI estimation methods operating at  $\Delta f = 30$  kHz cannot achieve the full rate even at high SNRs, which confirm the expected error floors in the BER results of Fig. 6(b) and (c). Nonetheless, Fig. 7(b) and (c) evidence that the CSI estimation methods for OFDM-based OTFS devised in Sec. II-E are capable of approaching to their ideal cases of perfect CSI at  $\Delta f' = 60$  kHz and outperforming OFDM, which confirm the BER results of Fig. 6(b) and (c).

### III. NONCOHERENT OTFS SYSTEM DESIGN

#### A. Noncoherent OTFS System Design Based on Differential V-BLAST

The OTFS input-output relationship of (20) is equivalent to a V-BLAST system having  $MN$  TAs and  $MN$  RAs. Therefore, we propose to conceive the noncoherent OTFS system based on a differential V-BLAST-like structure [39]–[41]. First of all, the differential encoding is performed for the  $\kappa$ -th element in  $\tilde{\mathbf{s}}$  for PSK signalling as:

$$\tilde{s}_{\kappa}^{\beta} = \tilde{s}_{\kappa}^{\beta-1} \tilde{x}_{\kappa}^{\beta}, \quad (33)$$

where  $\beta$  refers to the OTFS frame index, while we have vectorized the DD index  $\kappa = 0, \dots, MN - 1$  based on (20).  $\tilde{x}_{\kappa}^{\beta}$  refers to the modulated symbol that carries source information. For star/square QAM signalling, the absolute-amplitude differential encoding is performed based on [62]–[65]:

$$\tilde{s}_{\kappa}^{\beta} = \frac{1}{|\tilde{s}_{\kappa}^{\beta-1}|} \tilde{s}_{\kappa}^{\beta-1} \tilde{x}_{\kappa}^{\beta}, \quad (34)$$

where the amplitude of the previous symbol  $|\tilde{s}_{\kappa}^{\beta-1}|$  will be detected at the receiver based on decision-feedback. Following

$$\mathbb{C}(SNR) = M\Delta f \times \max_{\{p(\tilde{s}_\kappa = \tilde{s}^i)\}_{i=1}^{\mathcal{L}}} \sum_{i=1}^{\mathcal{L}} \int p(\tilde{\mathbf{z}}_\kappa | \tilde{s}^i) p(\tilde{s}^i) \log_2 \frac{p(\tilde{\mathbf{z}}_\kappa | \tilde{s}^i)}{\sum_{i'=1}^{\mathcal{L}} p(\tilde{\mathbf{z}}_\kappa | \tilde{s}^{i'}) p(\tilde{s}^{i'})} d\tilde{\mathbf{z}}_\kappa = \frac{M\Delta f}{\mathcal{L}} \sum_{i=1}^{\mathcal{L}} E \left[ \log_2 \frac{\mathcal{L} \times p(\tilde{\mathbf{z}}_\kappa | \tilde{s}^i)}{\sum_{i'=1}^{\mathcal{L}} p(\tilde{\mathbf{z}}_\kappa | \tilde{s}^{i'})} \right] \quad (31)$$

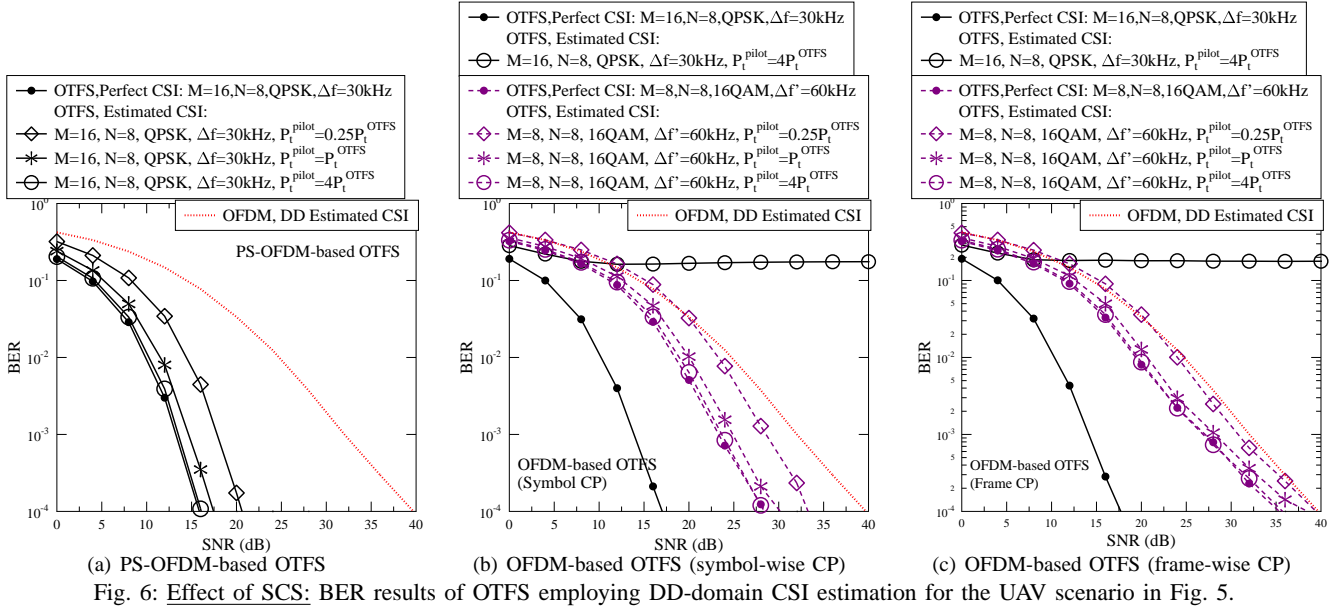


Fig. 6: Effect of SCS: BER results of OTFS employing DD-domain CSI estimation for the UAV scenario in Fig. 5.

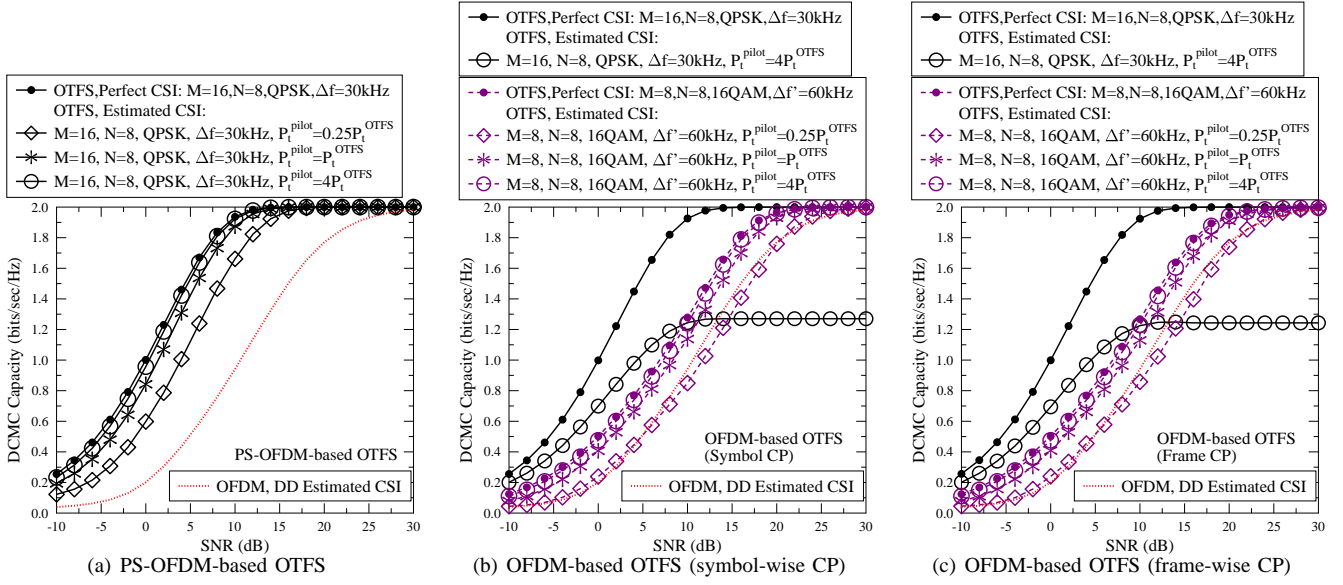


Fig. 7: Effect of SCS: DCMC capacity results of OTFS employing DD-domain CSI estimation for the UAV scenario.

this, the OTFS input-output model of (20) is further extended as:

$$\tilde{\mathbf{y}}^\beta = \tilde{\mathbf{H}}\tilde{\mathbf{s}}^\beta + \tilde{\mathbf{v}}^\beta = \sum_{\kappa=0}^{MN-1} \tilde{\mathbf{H}}_{-, \kappa} \tilde{s}_\kappa^\beta + \tilde{\mathbf{v}}^\beta = \sum_{\kappa=0}^{MN-1} \tilde{\mathbf{y}}_{\kappa}^\beta + \tilde{\mathbf{v}}^\beta, \quad (35)$$

where we have  $\tilde{\mathbf{y}}_{\kappa}^\beta = \tilde{\mathbf{H}}_{-, \kappa} \tilde{s}_\kappa^\beta$ . Based on (35), the DFDD for index  $\kappa$  may be expressed as:

$$\hat{\tilde{x}}_\kappa^\beta = \arg \min_{\tilde{x}_\kappa^\beta} \|\mathbf{w}_\kappa^H (\tilde{\mathbf{y}}^\beta - \tilde{x}_\kappa^\beta \tilde{\mathbf{y}}_{\text{ref}, \kappa}^{\beta-1})\|^2, \quad (36)$$

where  $\mathbf{w}_\kappa \in \mathcal{C}^{MN \times 1}$  refers to the filtering weights, while the reference signal vector  $\tilde{\mathbf{y}}_{\text{ref}, \kappa}^{\beta-1} \in \mathcal{C}^{MN \times 1}$  is constructed based on decision-feedbacks of  $\{\hat{\tilde{s}}_\kappa^{\beta-\eta}\}_{\eta=1}^{N_w-1}$  as seen in [7], [63], [66]–[68]. More explicitly, for non-recursive DFDD, the

reference signal vector is given by:

$$\begin{aligned} \text{PSK:} \quad \tilde{\mathbf{y}}_{\text{ref}, \kappa}^{\beta-1} &= \frac{1}{N_w-1} \hat{\tilde{s}}_\kappa^{\beta-1} \sum_{\eta=1}^{N_w-1} \left[ \left( \hat{\tilde{s}}_\kappa^{\beta-\eta} \right)^* \tilde{\mathbf{y}}^{\beta-\eta} \right], \\ \text{QAM:} \quad \tilde{\mathbf{y}}_{\text{ref}, \kappa}^{\beta-1} &= \frac{1}{N_w-1} \frac{\hat{\tilde{s}}_\kappa^{\beta-1}}{|\hat{\tilde{s}}_\kappa^{\beta-1}|} \sum_{\eta=1}^{N_w-1} \frac{\tilde{\mathbf{y}}^{\beta-\eta}}{\hat{\tilde{s}}_\kappa^{\beta-\eta}}, \end{aligned} \quad (37)$$

where  $N_w \geq 2$  denotes the DFDD window length. For recursive DFDD, the reference signal vector is constructed by:

$$\begin{aligned} \text{PSK:} \quad \tilde{\mathbf{y}}_{\text{ref}, \kappa}^{\beta-1} &= \xi \hat{\tilde{x}}_\kappa^{\beta-1} \tilde{\mathbf{y}}_{\text{ref}, \kappa}^{\beta-2} + (1-\xi) \tilde{\mathbf{y}}^{\beta-1}, \\ \text{QAM:} \quad \tilde{\mathbf{y}}_{\text{ref}, \kappa}^{\beta-1} &= \frac{1}{|\hat{\tilde{s}}_\kappa^{\beta-1}|} \left[ \xi \hat{\tilde{x}}_\kappa^{\beta-1} \tilde{\mathbf{y}}_{\text{ref}, \kappa}^{\beta-2} + (1-\xi) \tilde{\mathbf{y}}^{\beta-1} \right], \end{aligned} \quad (38)$$

where  $0 \leq \xi < 1$  denotes the DFDD forgetting factor. The DFDD performance improves upon increasing  $N_w$  and  $\xi$ , when the fading is near-constant.

Similar to noncoherent V-BLAST's inter-antenna interference, the noncoherent OTFS systems suffer from DD-domain

interference, which has to be mitigated without CSI knowledge. As shown in [39]–[41], the signal-to-interference-plus-noise-ratio (SINR) is defined as the ratio between the power of the desired filtered signal  $\mathbf{w}_\kappa^H \tilde{\mathbf{y}}_\kappa^\beta$  and that of the error signal  $\mathbf{w}_\kappa^H (\tilde{\mathbf{y}}^\beta - \tilde{\mathbf{y}}_\kappa^\beta)$ , which can be expressed as:

$$\text{SINR} = \frac{\mathbf{w}_\kappa^H (\mathbf{R}_{yy} - \mathbf{R}_{ee,\kappa}) \mathbf{w}_\kappa}{\mathbf{w}_\kappa^H \mathbf{R}_{ee,\kappa} \mathbf{w}_\kappa} = \frac{\mathbf{w}_\kappa^H \mathbf{R}_{yy} \mathbf{w}_\kappa}{\mathbf{w}_\kappa^H \mathbf{R}_{ee,\kappa} \mathbf{w}_\kappa}. \quad (39)$$

The  $(MN \times MN)$ -element correlation matrix of the received signal is given by:

$$\mathbf{R}_{yy} = E[\tilde{\mathbf{y}}^\beta (\tilde{\mathbf{y}}^\beta)^H], \quad (40)$$

which is averaged with respect to  $\beta$ . The  $(MN \times MN)$ -element correlation matrix of the error signal is formulated as:

$$\mathbf{R}_{ee,\kappa} = \chi E[(\tilde{\mathbf{y}}^\beta - \tilde{\mathbf{x}}_\kappa^\beta \tilde{\mathbf{y}}_{\text{ref},\kappa}^{\beta-1}) (\tilde{\mathbf{y}}^\beta - \tilde{\mathbf{x}}_\kappa^\beta \tilde{\mathbf{y}}_{\text{ref},\kappa}^{\beta-1})^H], \quad (41)$$

where we have  $\chi = 1 - \frac{1}{N_w}$  for non-recursive DFDD and  $\chi = \frac{1+\xi}{2}$  for recursive DFDD. Both  $\mathbf{R}_{yy}$  and  $\mathbf{R}_{ee,\kappa}$  may be obtained either from a training sequence or decision-feedback. As shown in [39]–[41], the optimization of (39) can be solved by using the method of Lagrange multipliers. The corresponding cost function is defined as  $\mathcal{J}(\mathbf{w}_\kappa) = \mathbf{w}_\kappa^H \mathbf{R}_{yy} \mathbf{w}_\kappa + \lambda_\kappa (\Upsilon - \mathbf{w}_\kappa^H \mathbf{R}_{ee,\kappa} \mathbf{w}_\kappa)$ , where  $\Upsilon > 0$  is an arbitrary positive constant, while  $\lambda_\kappa$  refers to the real-valued Lagrange multiplier. The differentiation of  $\frac{\partial \mathcal{J}(\mathbf{w}_\kappa)}{\partial \mathbf{w}_\kappa} = 0$  leads to the following generalized eigenvalue problem:

$$\mathbf{R}_{yy} \mathbf{w}_\kappa = \lambda_\kappa \mathbf{R}_{ee,\kappa} \mathbf{w}_\kappa, \quad (42)$$

where  $\lambda_\kappa$  and  $\mathbf{w}_\kappa$  correspond to the eigenvalue and eigenvector, respectively. Given the dimensions of  $\tilde{\mathbf{y}}^\beta \in \mathcal{C}^{MN \times 1}$  in (35), there is only one non-zero eigenvalue for the noncoherent OTFS using the V-BLAST model. In summary, upon solving (42) based on calculating the correlation metrics of (40) and (41), the filtering weights  $\mathbf{w}_\kappa$  is obtained for (36) without CSI.

### B. Noncoherent OTFS System Design Based on Multiplexed Differential STBC

Considering the equivalence between the OTFS DD-domain model and generic MIMO, we propose to partition the DD-domain modulated symbols into groups, where the orthogonal STBC is invoked in order to eliminate the DD-domain interference within each group. More explicitly, upon collecting  $N_G$  OTFS frames of (35), the  $(MN \times N_G)$ -dimensional OTFS input matrix  $\tilde{\mathbf{S}}^\beta = [\tilde{\mathbf{s}}^{\beta N_G}, \tilde{\mathbf{s}}^{\beta N_G+1}, \dots, \tilde{\mathbf{s}}^{(\beta+1)N_G-1}]$  can be partitioned into  $G$  groups of  $(N_G \times N_G)$ -element STBC codewords. For PSK, the differential STBC encoding for each group is given by [69]–[71]:

$$\tilde{\mathbf{s}}_g^\beta = \tilde{\mathbf{s}}_g^{\beta-1} \tilde{\mathbf{X}}_g^\beta, \quad (43)$$

where  $g = 0, \dots, G-1$  is the group index. Similarly, for QAM constellations, the differential STBC encoding of each group is expressed as [72]–[74]:

$$\tilde{\mathbf{s}}_g^\beta = \frac{\sqrt{N_G}}{\|\tilde{\mathbf{s}}_g^{\beta-1}\|} \tilde{\mathbf{s}}_g^{\beta-1} \tilde{\mathbf{X}}_g^\beta. \quad (44)$$

For example, the classic Alamouti codeword associated with  $N_G = 2$  is given by:

$$\tilde{\mathbf{X}}_g^\beta = \frac{1}{\sqrt{2}} \begin{bmatrix} x_1 & -x_2^* \\ x_2 & x_1^* \end{bmatrix}, \quad (45)$$

where  $x_1$  and  $x_2$  are PSK/QAM symbols, while the normalization of  $\frac{1}{\sqrt{N_G}} = \frac{1}{\sqrt{2}}$  ensures that the transmission power does

not grow with differential encoding of (43) and (44). We note that this normalization factor has to be scaled back for signal transmission. More explicitly, the DD-domain received signal can be expressed as:

$$\tilde{\mathbf{Y}}^\beta = \sqrt{N_G} \tilde{\mathbf{H}} \tilde{\mathbf{S}}^\beta + \tilde{\mathbf{V}}^\beta = \sqrt{N_G} \sum_{g=0}^{G-1} \tilde{\mathbf{H}}_g \tilde{\mathbf{S}}_g^\beta + \tilde{\mathbf{V}}^\beta = \sum_{g=0}^{G-1} \tilde{\mathbf{Y}}_g + \tilde{\mathbf{V}}^\beta, \quad (46)$$

where  $\tilde{\mathbf{Y}}^\beta \in \mathcal{C}^{MN \times N_G}$  and  $\tilde{\mathbf{S}}^\beta \in \mathcal{C}^{MN \times N_G}$  model a total of  $N_G$  OTFS transmit and receive frames in the form of (35), respectively. The fading submatrix of the  $g$ -th group,  $\tilde{\mathbf{H}}_g \in \mathcal{C}^{MN \times N_G}$ , is taken from the  $gN_G$ -th to the  $(gN_G + N_G - 1)$ -th columns of  $\tilde{\mathbf{H}}$ . Accordingly,  $\tilde{\mathbf{S}}_g \in \mathcal{C}^{N_G \times N_G}$  is taken from the  $gN_G$ -th to the  $(gN_G + N_G - 1)$ -th rows of  $\tilde{\mathbf{S}}$ .

As a result, the DFDD performed for the  $g$ -th group is given by:

$$\hat{\tilde{\mathbf{X}}}_g^\beta = \arg \min_{\tilde{\mathbf{X}}_g^\beta} \|\mathbf{W}_g^H (\tilde{\mathbf{Y}}^\beta - \tilde{\mathbf{X}}_g^\beta \tilde{\mathbf{Y}}_{\text{ref},g}^{\beta-1})\|^2, \quad (47)$$

where  $\mathbf{W}_g \in \mathcal{C}^{MN \times N_G}$  and  $\tilde{\mathbf{Y}}_{\text{ref},g}^{\beta-1} \in \mathcal{C}^{MN \times N_G}$  refer to the filter and reference matrices, respectively. For the non-recursive DFDD, the reference signal matrix is constructed based on the decision-feedbacks  $\{\hat{\tilde{\mathbf{S}}}_g^{\beta-\eta}\}_{\eta=1}^{N_w-1}$  as:

$$\begin{aligned} \text{PSK: } \tilde{\mathbf{Y}}_{\text{ref},g}^{\beta-1} &= \frac{1}{N_w-1} \left[ \sum_{\eta=1}^{N_w-1} \tilde{\mathbf{Y}}^{\beta-\eta} (\hat{\tilde{\mathbf{S}}}_g^{\beta-\eta})^H \right] \hat{\tilde{\mathbf{S}}}_g^{\beta-1}, \\ \text{QAM: } \tilde{\mathbf{Y}}_{\text{ref},g}^{\beta-1} &= \frac{\sqrt{N_G}}{N_w-1} \left[ \sum_{\eta=1}^{N_w-1} \tilde{\mathbf{Y}}^{\beta-\eta} (\hat{\tilde{\mathbf{S}}}_g^{\beta-\eta})^H / \|\hat{\tilde{\mathbf{S}}}_g^{\beta-\eta}\| \right] \hat{\tilde{\mathbf{S}}}_g^{\beta-1} / \|\hat{\tilde{\mathbf{S}}}_g^{\beta-1}\|. \end{aligned} \quad (48)$$

For the recursive DFDD, the reference signal matrix is expressed as:

$$\begin{aligned} \text{PSK: } \tilde{\mathbf{Y}}_{\text{ref},g}^{\beta-1} &= \xi \tilde{\mathbf{Y}}_{\text{ref},g}^{\beta-2} \hat{\tilde{\mathbf{X}}}_g^{\beta-1} + (1-\xi) \tilde{\mathbf{Y}}^{\beta-1}, \\ \text{QAM: } \tilde{\mathbf{Y}}_{\text{ref},g}^{\beta-1} &= \sqrt{N_G} \left[ \xi \tilde{\mathbf{Y}}_{\text{ref},g}^{\beta-2} \hat{\tilde{\mathbf{X}}}_g^{\beta-1} + (1-\xi) \tilde{\mathbf{Y}}^{\beta-1} \right] / \|\hat{\tilde{\mathbf{X}}}_g^{\beta-1}\|. \end{aligned} \quad (49)$$

Thanks to the orthogonality of the STBC design, there is no interference within each group of STBC codeword  $\tilde{\mathbf{X}}_g^\beta$ . However, the interference between groups still has to be mitigated. Based on (46), the generalized eigenvalue problem of (42) is revised as:

$$\mathbf{R}_{yy} \mathbf{w}_g = \lambda_g \mathbf{R}_{ee,g} \mathbf{w}_g, \quad (50)$$

where there are  $N_G$  eigenvalues for  $\lambda_g$  based on the dimension of  $\tilde{\mathbf{Y}}^\beta$  of (46). The  $(MN \times MN)$ -element correlation matrix of the received signal in (53) is given by:

$$\mathbf{R}_{yy} = E[\tilde{\mathbf{Y}}^\beta (\tilde{\mathbf{Y}}^\beta)^H]. \quad (51)$$

Furthermore, the  $(MN \times MN)$ -element correlation matrix of the error signal is formulated by:

$$\mathbf{R}_{ee,g} = \chi E[(\tilde{\mathbf{Y}}^\beta - \tilde{\mathbf{Y}}_{\text{ref},g}^{\beta-1} \tilde{\mathbf{X}}_g^\beta) (\tilde{\mathbf{Y}}^\beta - \tilde{\mathbf{Y}}_{\text{ref},g}^{\beta-1} \tilde{\mathbf{X}}_g^\beta)^H]. \quad (52)$$

As a result, the  $N_G$  columns in  $\mathbf{W}_g$  of (47) correspond to  $N_G$  eigenvectors of (53) as given by:

$$\mathbf{W}_g = [\mathbf{w}_g^0, \mathbf{w}_g^1, \dots, \mathbf{w}_g^{N_G-1}]. \quad (53)$$

In summary, the noncoherent OTFS algorithms are summarized in Table IV, where a training phase is assumed for obtaining the correlation matrices  $\mathbf{R}_{yy}$  and  $\mathbf{R}_{ee,\kappa}$  of (40) and (41), respectively, as well as  $\mathbf{R}_{yy}$  and  $\mathbf{R}_{ee,g}$  of (51) and (52), respectively. The training phase is limited to be lower than 10% of the entire OTFS transmission, and the training

TABLE IV: Summary of noncoherent OTFS using V-BLAST and STBC codewords.

Noncoherent OTFS using V-BLAST	Noncoherent OTFS using STBC
<b>Input:</b> training $\tilde{x}_\kappa^\beta$ and data-carrying $\tilde{x}_\kappa^\beta$ . <b>Output:</b> DFDD decisions on data-carrying $\tilde{x}_\kappa^\beta$ . <b>Training phase for obtaining DFDD weights:</b> <b>Step T.1:</b> Diff. encoding of (33) and (34) with training $\tilde{x}_\kappa^\beta$ . <b>Step T.2:</b> Received signal modelling of (35). <b>Step T.3:</b> Obtaining $\mathbf{R}_{yy}$ of (40) and $\mathbf{R}_{ee,\kappa}$ of (41). <b>Step T.4:</b> Obtaining DFDD weights $\mathbf{w}_\kappa$ based on (42). <b>Data transmission phase and DFDD:</b> <b>Step D.1:</b> Diff. encoding of (33) and (34) with data $\tilde{x}_\kappa^\beta$ . <b>Step D.2:</b> Received signal modelling of (35). <b>Step D.3:</b> DFDD of (36) for detecting data $\tilde{x}_\kappa^\beta$ .	<b>Input:</b> training $\tilde{\mathbf{X}}_g^\beta$ and data-carrying $\tilde{\mathbf{X}}_g^\beta$ . <b>Output:</b> DFDD decisions on data-carrying $\tilde{\mathbf{X}}_g^\beta$ . <b>Training phase for obtaining DFDD weights:</b> <b>Step T.1:</b> Diff. encoding of (43) and (44) with training $\tilde{\mathbf{X}}_g^\beta$ . <b>Step T.2:</b> Received signal modelling of (46). <b>Step T.3:</b> Obtaining $\mathbf{R}_{yy}$ of (51) and $\mathbf{R}_{ee,g}$ of (52). <b>Step T.4:</b> Obtaining DFDD weights $\mathbf{W}_g$ based on (53). <b>Data transmission phase and DFDD:</b> <b>Step D.1:</b> Diff. encoding of (43) and (44) with data $\tilde{\mathbf{X}}_g^\beta$ . <b>Step D.2:</b> Received signal modelling of (46). <b>Step D.3:</b> DFDD of (47) for detecting data $\tilde{\mathbf{X}}_g^\beta$ .

overhead can be mitigated using decision-feedback assisted by channel coding, which will be further discussed in Sec. III-C.

### C. Simulation Results for Noncoherent OTFS

First of all, the DFDD parameters are investigated in Fig. 8. As discussed in Sec. III-A, the correlation matrices  $\mathbf{R}_{yy}$  and  $\mathbf{R}_{ee,\kappa}$  of (41) are generally assumed to be obtained either from a training sequence or decision-feedback [39]–[41]. Reliable data-aided decision-feedback is often assisted by channel coding and this also improves the CSI estimation of coherent OTFS [21], [75], which leads to a different trade-off that is beyond the scope of this paper. Hence having a training sequence is assumed here. In order to ensure the accuracy of correlation evaluation, the fading is assumed to be time-varying in the TF-domain but quasi-static in the DD-domain. In order to achieve this, the following stringent conditions are required for this work:

- The training overhead is lower than 10%.
- The distance travelled during a sequence of OTFS transmission is lower than 1% of the coverage distance.
- In this way, the variations in path-loss, angle-of-arrival/departure (AoA/AoD) and vehicular speed are negligible in comparison to the overall coverage range.

These limitations inevitably results in relatively small values for  $M$  and  $N$  for noncoherent OTFS, making it suitable for low-rate but reliable alternatives to coherent schemes in the high-Doppler train and aeronautical communication scenarios<sup>2</sup>. Fig. 8(a) demonstrates that for the train scenario associated with  $M = 8$  and  $N = 4$ , the training sequence length of 200 OTFS frames is sufficient. Fig. 8(b) demonstrates that for the UAV scenario associated with  $M = 16$  and  $N = 8$ , the training sequence length of 600 OTFS frames is chosen. For the high-speed train of Fig. 5 associated with the speed of 540 km/s, having the SCS of  $\Delta f = 30$  kHz,  $N = 4$  and a training overhead of 10%, a sequence of OTFS transmission would take merely  $\frac{N \times 2000}{\Delta f} = 0.27$  seconds, and the distance travelled by the train is 40 meters. This is much lower than 1% of the coverage distance of 10~20 km (1% at 100~200 m). The UAV coverage in Fig. 5 allows abundant OTFS transmission time, despite the high vehicular speed, where the distance traveled at Mach 7 over 0.8 seconds is

given by 1.92 km, which is also substantially lower than the coverage distance of 200 nautical miles ( $\approx 370$  km). Moreover, Fig. 8(c) and (d) demonstrate that  $N_w = 6$  and  $\xi = 0.9$  are sufficient for non-recursive DFDD and recursive DFDD, which are the parameters used in the rest of this paper. We note that the pilot overhead of coherent OTFS schemes and the training overhead of the noncoherent OTFS schemes are both normalized into SNR for all performance results in this paper.

For the coherent versus noncoherent comparison, Fig. 9 portrays the BER results of coherent OFDM-based OTFS employing DD-domain CSI estimation and noncoherent OFDM-based OTFS using DFDD. Specifically, Fig. 9(a) is for the train scenario using frame-wise CP with  $R = 2.0$ , while Fig. 9(b) and Fig. 9(c) are for the UAV scenario using symbol-wise CP with  $R = 2.0$  and  $R = 4.0$ , respectively. It can be seen in Fig. 9(a)-(c) that first of all, coherent OTFS relying on perfect CSI is capable of achieving the best performance at  $\Delta f = 30$  kHz. Secondly, as expected, the CSI estimation techniques operating at  $\Delta f = 30$  kHz exhibit error floors for both the train scenario associated with  $\vartheta_{\max} = 19.25$  kHz and the UAV scenario associated with  $\vartheta_{\max} = 20.75$  kHz, as evidenced by Fig. 9(a)-(c). Fourthly, the practical CSI estimation techniques have to double the SCS  $\Delta f' = 2\Delta f > 2\vartheta_{\max}$ , where the number of SC needs to be reduced and the PSK/QAM modulation level has to be increased in order to convey the same throughput given the same system bandwidth. By contrast, the noncoherent OTFS schemes using DFDD are capable of retaining  $\Delta f = 30$  kHz and achieving substantially improved performance than their coherent OTFS counterparts using estimated CSI, as demonstrated by Fig. 9(a)-(c).

The BER results of Fig. 9 are further confirmed by the DCMC capacity results of Fig. 10. The DCMC capacity of noncoherent OTFS schemes is also evaluated based on (31), where the conditional probability is given by:

$$p(\tilde{\mathbf{z}}_\kappa | \tilde{s}^i) = \frac{1}{\pi \tilde{N}_{0,\kappa}} \exp\left(-\frac{|\tilde{\mathbf{z}}_\kappa - \tilde{\mathbf{z}}_{\text{ref},\kappa} \tilde{s}^i|^2}{\tilde{N}_{0,\kappa}}\right), \quad (54)$$

where we have  $\tilde{\mathbf{z}}_\kappa = \mathbf{w}_\kappa^H \tilde{\mathbf{y}}^\beta$ ,  $\tilde{\mathbf{z}}_{\text{ref},\kappa} = \mathbf{w}_\kappa^H \tilde{\mathbf{y}}_{\text{ref},\kappa}^{\beta-1}$  and  $\tilde{N}_{0,\kappa} = N_0 \|\mathbf{w}_\kappa\|^2$ . Fig. 10(a)-(c) confirm the BER results of Fig. 9(a)-(c), indicating that the coherent OTFS scheme relying on perfect CSI at  $\Delta f = 30$  kHz achieve the best DCMC capacity, which is manifested by the fact that the case of perfect CSI achieves the full rate at the lowest SNR. The CSI estimation techniques operating at  $\Delta f = 30$  kHz cannot achieve the full rate even at high SNR in the DCMC capacity results of Fig. 10(a)-(c), which results in the error floors observed in

<sup>2</sup>We note that the existing aircraft communications addressing and reporting system (ACARS), the automatic dependent surveillance (ADS) and the L-band digital aeronautical communications system (L-DACS) deployed on airplanes have the low rates of 2.4 KBaud [76], 1 MBaud [77] and 625 KBaud [55], respectively, where the reduced SCS requirement of the proposed noncoherent OTFS system becomes especially beneficial.

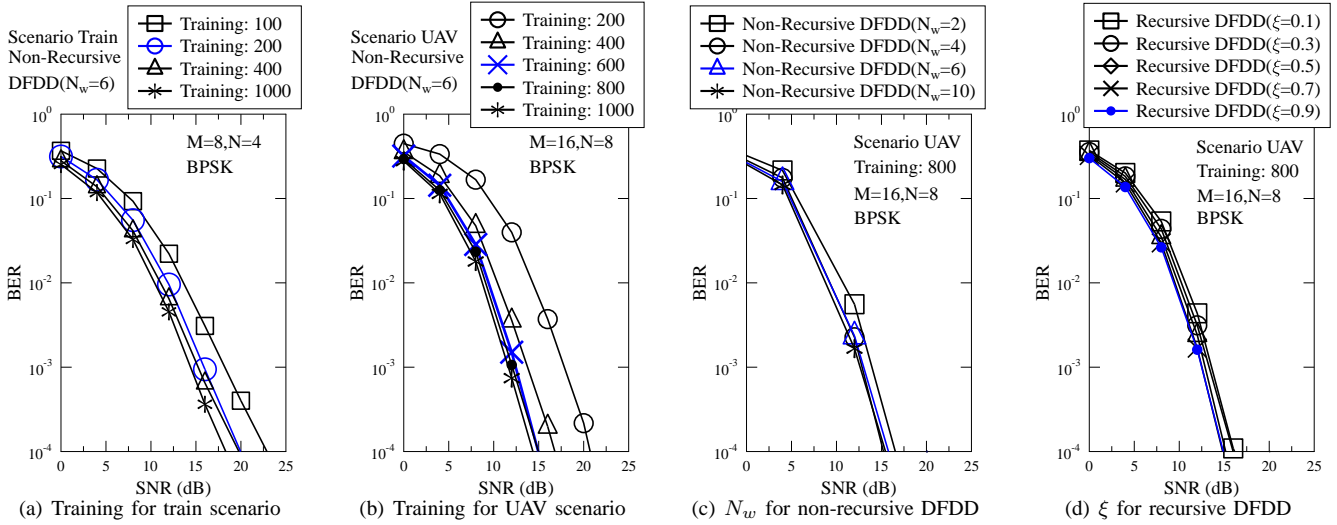


Fig. 8: DFDD Parameters: BER results of DFDD assisted noncoherent OFDM-based OTFS with symbol-wise CP for the train and UAV scenarios summarized in Fig. 5.

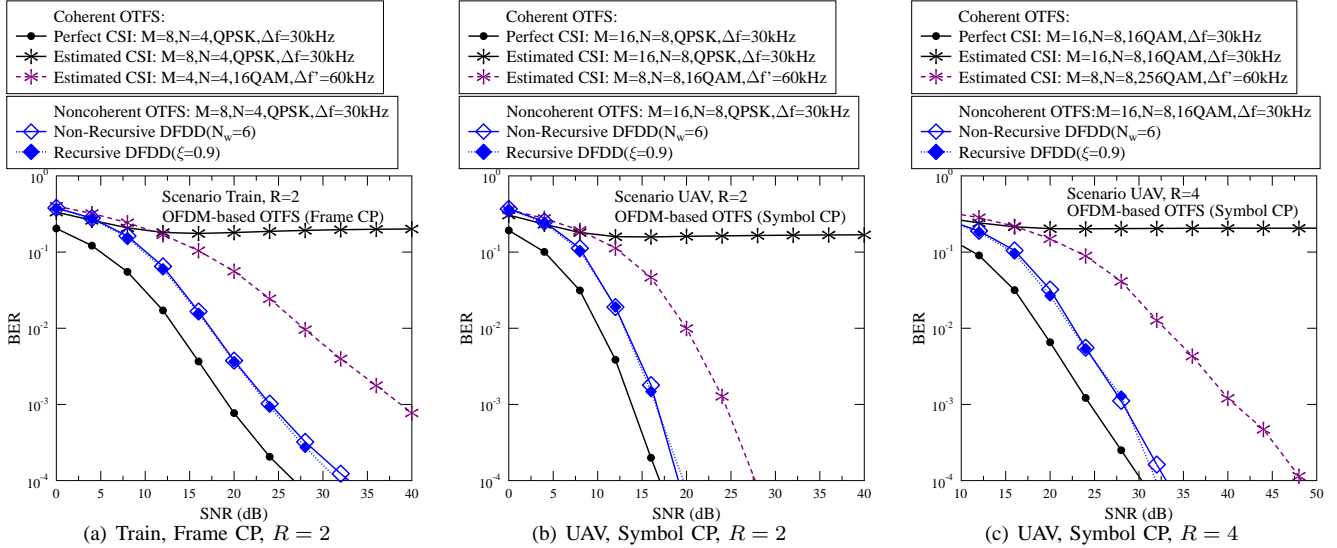


Fig. 9: Coherent versus Noncoherent: BER results of coherent OFDM-based OTFS employing DD-domain CSI estimation and noncoherent OFDM-based OTFS using DFDD.

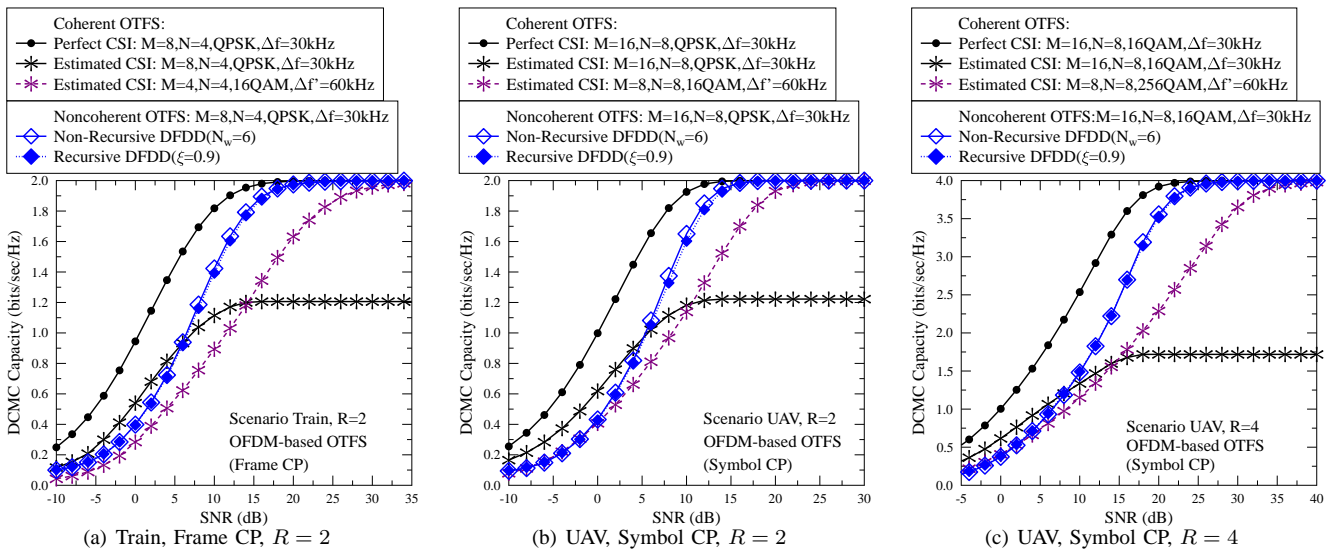


Fig. 10: Coherent versus Noncoherent: DCMC capacity results of coherent OFDM-based OTFS employing DD-domain CSI estimation and noncoherent OFDM-based OTFS using DFDD.

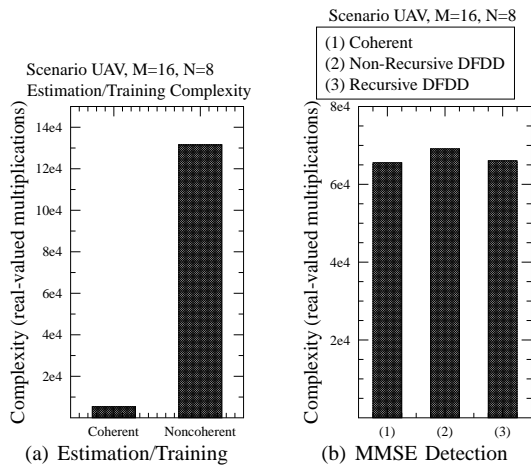


Fig. 12: Complexity: Complexity comparison between coherent OTFS and noncoherent OTFS in terms of the number of real-valued multiplications, where we have  $M = 16$ ,  $N = 8$  and  $N_w = 6$ .

the BER results of Fig. 9(a)-(c). Fig. 10(a)-(c) further confirm that the noncoherent OTFS schemes using DFDD outperform their practical coherent OTFS counterparts relying on CSI estimation.

Fig. 11 portrays the BER results of noncoherent OTFS systems using V-BLAST and STBC codewords in the DD-domain. It is demonstrated in Fig. 11 that Alamouti's STBC codeword helps to improve the performance of noncoherent OFDM-based OTFS systems. Nonetheless, the STBC's performance improvements are eroded, as  $M$  and  $R$  increase in Figs. 11(a)-(d). This is due to the fact that Alamouti's STBC structure of (45) suffers from a throughput loss, hence we have to increase the modulation order from BPSK to QPSK for  $R = 1$  in Fig. 11(a)-(c) and from QPSK to 16QAM for  $R = 2$  in Fig. 11(d). It may be expected that the full-diversity full-rate STBCs may achieve a further improved performance at the cost of increased interference [78]–[82], which may be further mitigated by index modulation designs [83]–[87]. These applications are beyond the scope of this treatise, and they are set aside for our future research.

Finally, Fig. 12 portrays the complexity comparison between coherent OFDM-based OTFS using CSI estimation and noncoherent OFDM-based OTFS using DFDD. First of all, we note that the noncoherent detection in the TF-domain suffers from time-varying fading channels, which lead to high-complexity noncoherent detectors that require matrix inversions [7], [35]–[38]. These matrix inversions are eliminated by the proposed noncoherent OTFS schemes using recursive and non-recursive DFDD, thanks to the time-invariant nature of the DD-domain fading. Nonetheless, Fig. 12(a) demonstrates that the estimation of the correlation matrices  $\mathbf{R}_{yy}$  and  $\mathbf{R}_{ee,\kappa}$  of (41) based on a training sequence imposes substantially higher complexity than the coherent CSI estimation technique devised in Sec. II-E. One may conclude that the improved performance of noncoherent OTFS in Figs. 9 and 10 is achieved at the cost of a higher complexity, as shown in Fig. 12. Nonetheless, we note that the training sequence only takes up less than 10% of the OTFS transmission, where the data detection contributes to the majority of the receiver complexity. In this regard, Fig. 12(b) demonstrates that the coherent and noncoherent

MMSE detectors exhibit similar complexity level, albeit the non-recursive DFDD still has a higher complexity, which is reduced by the recursive DFDD design.

#### IV. CONCLUSIONS AND FUTURE WORKS

We devised practical CSI estimation techniques and we demonstrated that practical OFDM-based OTFS systems have to double their SCS  $\Delta f' = 2\Delta f > 2\vartheta_{\max}$ . In order to mitigate this problem, new noncoherent OTFS systems were conceived for the first time in the literature, which is capable of operating at the minimum SCS requirement of  $\Delta f > \vartheta_{\max}$  and outperforming their coherent OTFS counterparts relying on estimated CSI, at the cost of a relatively smaller OTFS input-output dimension and an increased training complexity.

#### REFERENCES

- [1] J. Liu, Y. Shi, Z. Fadlullah, and N. Kato, "Space-air-ground integrated network: A survey," *IEEE Commun. Surveys Tuts.*, vol. 20, no. 4, pp. 2714–2741, 2018.
- [2] C. Xu, J. Zhang, T. Bai, P. Botsinis, R. G. Maunder, R. Zhang, and L. Hanzo, "Adaptive coherent/non-coherent single/multiple-antenna aided channel coded ground-to-air aeronautical communication," *IEEE Trans. Commun.*, vol. 67, no. 2, pp. 1099–1116, 2019.
- [3] C. Xu, T. Bai, J. Zhang, R. Rajashekar, R. G. Maunder, Z. Wang, and L. Hanzo, "Adaptive coherent/non-coherent spatial modulation aided unmanned aircraft systems," *IEEE Wireless Commun.*, vol. 26, no. 4, pp. 170–177, 2019.
- [4] X. Huang, J. Zhang, R. Liu, Y. Guo, and L. Hanzo, "Airplane-aided integrated networking for 6G wireless: Will it work?," *IEEE Veh. Technol. Mag.*, vol. 14, no. 3, pp. 84–91, 2019.
- [5] S. Dang, O. Amin, B. Shihada, and M. Alouini, "What should 6G be?," *Nat. Electron.*, vol. 3, pp. 20–29, 2020.
- [6] W. Saad, M. Bennis, and M. Chen, "A vision of 6G wireless systems: Applications, trends, technologies, and open research problems," *IEEE Network*, vol. 34, no. 3, pp. 134–142, 2020.
- [7] C. Xu, N. Ishikawa, R. Rajashekar, S. Sugiura, R. G. Maunder, Z. Wang, L. Yang, and L. Hanzo, "Sixty years of coherent versus non-coherent tradeoffs and the road from 5G to wireless futures," *IEEE Access*, vol. 7, pp. 178246–178299, 2019.
- [8] ITU *Measuring digital development: Facts and figures 2021* [Online]. Available: <https://www.itu.int/en/ITU-D/Statistics/Documents/facts/FactsFigures2021.pdf>.
- [9] M. Shafi, A. Molisch, P. Smith, T. Haustein, P. Zhu, P. D. Silva, F. Tufvesson, A. Benjebbour, and G. Wunder, "5G: A tutorial overview of standards, trials, challenges, deployment, and practice," *IEEE J. Sel. Areas Commun.*, vol. 35, no. 6, pp. 1201–1221, 2017.
- [10] A. Guidotti, A. Vanelli-Coralli, M. Conti, S. Andrenacci, S. Chatzinotas, N. Maturo, B. Evans, A. Awoseyila, A. Ugolini, T. Foggi, L. Gaudio, N. Alagha, and S. Cioni, "Architectures and key technical challenges for 5G systems incorporating satellites," *IEEE Trans. Veh. Technol.*, vol. 68, no. 3, pp. 2624–2639, 2019.
- [11] B. Ai, A. Molisch, M. Rupp, and Z. Zhong, "5G key technologies for smart railways," *Proc. IEEE*, vol. 108, no. 6, pp. 856–893, 2020.
- [12] L. Hanzo, Y. Akhtman, L. Wang, and M. Jiang, *MIMO-OFDM for LTE, WiFi and WiMAX: Coherent versus Non-coherent and Cooperative Turbo Transceivers*. John Wiley & Sons, 2011.
- [13] R. Hadani, S. Rakib, M. Tsatsanis, A. Monk, A. Goldsmith, A. Molisch, and R. Calderbank, "Orthogonal time frequency space modulation," in *2017 IEEE Wireless Communications and Networking Conference (WCNC)*, pp. 1–6, 2017.
- [14] Z. Wei, W. Yuan, S. Li, J. Yuan, G. Bharatula, R. Hadani, and L. Hanzo, "Orthogonal time-frequency space modulation: A promising next-generation waveform," *IEEE Wireless Commun.*, vol. 28, no. 4, pp. 136–144, 2021.
- [15] S. Mohammed, "Derivation of OTFS modulation from first principles," *IEEE Trans. Veh. Technol.*, vol. 70, no. 8, pp. 7619–7636, 2021.
- [16] A. Farhang, A. RezazadehReyhani, L. Doyle, and B. Farhang-Boroujeny, "Low complexity modem structure for OFDM-based orthogonal time frequency space modulation," *IEEE Wireless Commun. Lett.*, vol. 7, no. 3, pp. 344–347, 2018.
- [17] P. Raviteja, Y. Hong, E. Viterbo, and E. Biglieri, "Practical pulse-shaping waveforms for reduced-cyclic-prefix OTFS," *IEEE Trans. Veh. Technol.*, vol. 68, no. 1, pp. 957–961, 2019.



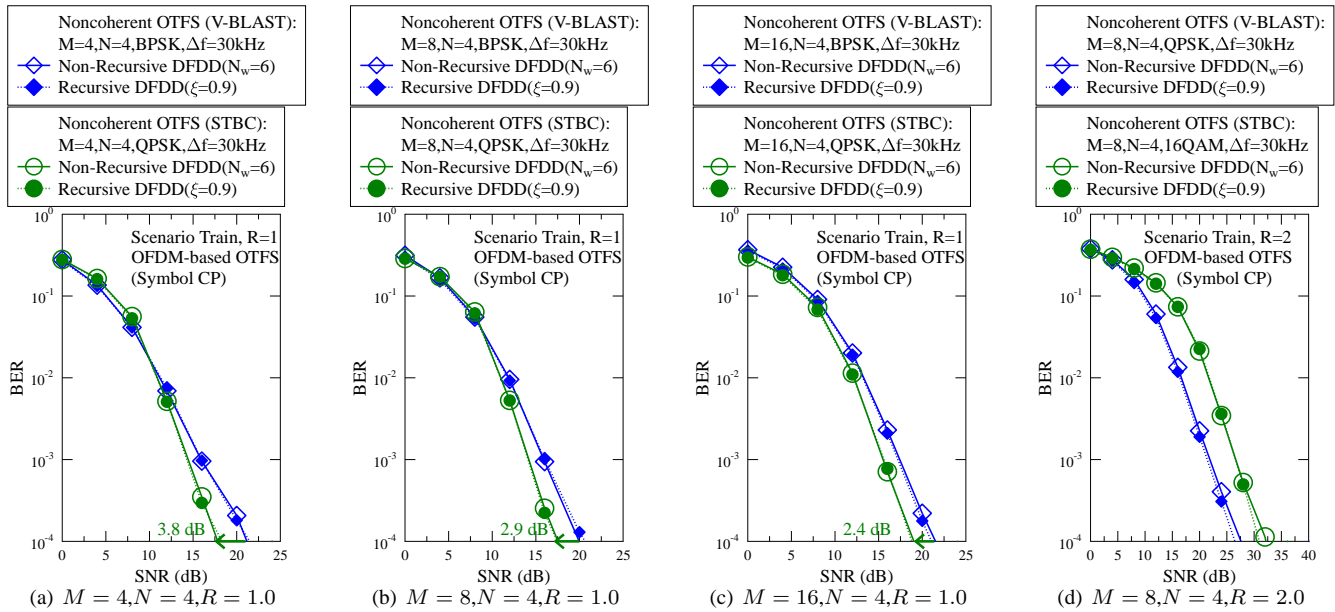


Fig. 11: V-BLAST versus STBC: BER results of noncoherent OTFS systems using V-BLAST and STBC codewords in the DD-domain.

- [18] Z. Wei, W. Yuan, S. Li, J. Yuan, and D. Ng, "Transmitter and receiver window designs for orthogonal time-frequency space modulation," *IEEE Trans. Commun.*, vol. 69, no. 4, pp. 2207–2223, 2021.
- [19] G. Surabhi, R. Augustine, and A. Chockalingam, "On the diversity of uncoded OTFS modulation in doubly-dispersive channels," *IEEE Trans. Wireless Commun.*, vol. 18, no. 6, pp. 3049–3063, 2019.
- [20] P. Raviteja, Y. Hong, E. Viterbo, and E. Biglieri, "Effective diversity of OTFS modulation," *IEEE Wireless Commun. Lett.*, vol. 9, no. 2, pp. 249–253, 2020.
- [21] S. Li, J. Yuan, W. Yuan, Z. Wei, B. Bai, and D. Ng, "Performance analysis of coded OTFS systems over high-mobility channels," *IEEE Trans. Wireless Commun.*, vol. 20, no. 9, pp. 6033–6048, 2021.
- [22] P. Raviteja, K. T. Phan, and Y. Hong, "Embedded pilot-aided channel estimation for OTFS in delay-doppler channels," *IEEE Trans. Veh. Technol.*, vol. 68, no. 5, pp. 4906–4917, 2019.
- [23] W. Shen, L. Dai, J. An, P. Fan, and R. Heath, "Channel estimation for orthogonal time frequency space (OTFS) massive MIMO," *IEEE Trans. Signal Process.*, vol. 67, no. 16, pp. 4204–4217, 2019.
- [24] A. RezazadehReyhani, A. Farhang, M. Ji, R. Chen, and B. Farhang-Boroujeny, "Analysis of discrete-time MIMO OFDM-based orthogonal time frequency space modulation," in *IEEE International Conference on Communications (ICC)*, 2018.
- [25] V. Khammammetti and S. K. Mohammed, "OTFS-based multiple-access in high Doppler and delay spread wireless channels," *IEEE Wireless Commun. Lett.*, vol. 8, no. 2, pp. 528–531, 2019.
- [26] G. Surabhi and A. Chockalingam, "Low-complexity linear equalization for OTFS modulation," *IEEE Commun. Lett.*, vol. 24, no. 2, pp. 330–334, 2020.
- [27] P. Raviteja, K. Phan, Y. Hong, and E. Viterbo, "Interference cancellation and iterative detection for orthogonal time frequency space modulation," *IEEE Trans. Wireless Commun.*, vol. 17, no. 10, pp. 6501–6515, 2018.
- [28] W. Yuan, Z. Wei, J. Yuan, and D. W. K. Ng, "A simple variational Bayes detector for orthogonal time frequency space (OTFS) modulation," *IEEE Trans. Veh. Technol.*, vol. 69, no. 7, pp. 7976–7980, 2020.
- [29] L. Xiang, Y. Liu, L. Yang, and L. Hanzo, "Gaussian approximate message passing detection of orthogonal time frequency space modulation," *IEEE Trans. Veh. Technol.*, vol. 70, no. 10, pp. 10999–11004, 2021.
- [30] S. Tiwari, S. Das, and V. Rangamgari, "Low complexity LMMSE receiver for OTFS," *IEEE Commun. Lett.*, vol. 23, no. 12, pp. 2205–2209, 2019.
- [31] P. Singh, A. Gupta, H. B. Mishra, and R. Budhiraja, "Low-complexity ZF/MMSE MIMO-OTFS receivers for high-speed vehicular communication," *IEEE Open J. Commun. Soc.*, vol. 3, pp. 209–227, 2022.
- [32] F. Liu, Z. Yuan, Q. Guo, Z. Wang, and P. Sun, "Message passing-based structured sparse signal recovery for estimation of OTFS channels with fractional Doppler shifts," *IEEE Trans. Wireless Commun.*, vol. 20, no. 12, pp. 7773–7785, 2021.
- [33] Z. Wei, W. Yuan, S. Li, J. Yuan, and D. Ng, "Off-grid channel estimation with sparse Bayesian learning for OTFS systems," *IEEE Trans. Wireless Commun.*, vol. 21, no. 9, pp. 7407–7426, 2022.
- [34] X. Wang, W. Shen, C. Xing, J. An, and L. Hanzo, "Joint Bayesian channel estimation and data detection for OTFS systems in LEO satellite communications," *IEEE Trans. Commun.*, vol. 70, no. 7, pp. 4386–4399, 2022.
- [35] D. Divsalar and M. K. Simon, "Maximum-likelihood differential detection of uncoded and trellis coded amplitude phase modulation over AWGN and fading channels—metrics and performance," *IEEE Trans. Commun.*, vol. 42, pp. 76–89, 1994.
- [36] J. Wu and P. Fan, "A survey on high mobility wireless communications: Challenges, opportunities and solutions," *IEEE Access*, vol. 4, pp. 450–476, 2016.
- [37] L. Wang, L. Li, C. Xu, D. Liang, S. X. Ng, and L. Hanzo, "Multiple-symbol joint signal processing for differentially encoded single- and multi-carrier communications: Principles, designs and applications," *IEEE Commun. Surveys Tuts.*, vol. 16, no. 2, pp. 689–712, 2014.
- [38] L. Hanzo, Y. Akhtman, L. Wang, and M. Jiang, *MIMO-OFDM for LTE, Wi-Fi and WiMAX: Coherent versus Non-coherent and Cooperative Turbo Transceivers*. Wiley-IEEE Press, 2011.
- [39] S. K. Cheung and R. Schober, "Differential spatial multiplexing," *IEEE Trans. Wireless Commun.*, vol. 5, no. 8, pp. 2127–2135, 2006.
- [40] L. Wang and L. Hanzo, "Differential interference suppression for SDMA-OFDM based on joint multiple-symbol filtering and detection," *IEEE Trans. Veh. Technol.*, vol. 60, no. 9, pp. 4656–4662, 2011.
- [41] L. Li, L. Wang, and L. Hanzo, "Differential interference suppression aided three-stage concatenated successive relaying," *IEEE Trans. Commun.*, vol. 60, no. 8, pp. 2146–2155, 2012.
- [42] L. Shi, T. Wang, Z. Mei, J. Li, and X.-G. Xia, "Revisiting non-coherent detection of differential PSK: A factor graph perspective," *IEEE Commun. Lett.*, vol. 27, no. 2, pp. 701–705, 2023.
- [43] R. Rajashekar, C. Xu, N. Ishikawa, L.-L. Yang, and L. Hanzo, "Sub-carrier subset selection-aided transmit precoding achieves full-diversity in index modulation," *IEEE Trans. Veh. Technol.*, vol. 68, no. 11, pp. 11031–11041, 2019.
- [44] C. Xu, Y. Xiong, N. Ishikawa, R. Rajashekar, S. Sugiura, Z. Wang, S. X. Ng, L.-L. Yang, and L. Hanzo, "Space-, time- and frequency-domain index modulation for next-generation wireless: A unified single-/multi-carrier and single-/multi-RF MIMO framework," *IEEE Trans. Wireless Commun.*, vol. 20, no. 6, pp. 3847–3864, 2021.
- [45] R. H. Clarke, "A statistical theory of mobile radio reception," *Bell Labs Technical Journal*, vol. 47, pp. 957–1000, 1968.
- [46] W. C. Jakes, *Microwave mobile communications*. John Wiley & Sons, 1975.
- [47] M. K. Ramachandran and A. Chockalingam, "MIMO-OTFS in high-doppler fading channels: Signal detection and channel estimation," in *2018 IEEE Global Communications Conference (GLOBECOM)*, pp. 206–212, 2018.
- [48] C. Xu, X. Zuo, S. X. Ng, R. G. Maunder, and L. Hanzo, "Reduced-complexity soft-decision multiple-symbol differential sphere detection," *IEEE Trans. Commun.*, vol. 63, no. 9, pp. 3275–3289, 2015.



- [49] C. Xu, J. An, T. Bai, L. Xiang, S. Sugiura, R. Maunder, L. Yang, and L. Hanzo, "Reconfigurable intelligent surface assisted multi-carrier wireless systems for doubly selective high-mobility Ricean channels," *IEEE Trans. Veh. Technol.*, vol. 71, no. 4, pp. 4023–4041, 2022.
- [50] K. Guan, B. Ai, B. Peng, D. He, G. Li, J. Yang, Z. Zhong, and T. Kurner, "Towards realistic high-speed train channels at 5G millimeter-wave bandpart I: Paradigm, significance analysis, and scenario reconstruction," *IEEE Trans. Veh. Technol.*, vol. 67, no. 10, pp. 9112–9128, 2018.
- [51] K. Guan, B. Ai, B. Peng, D. He, G. Li, J. Yang, Z. Zhong, and T. Kurner, "Towards realistic high-speed train channels at 5G millimeter-wave bandpart II: Case study for paradigm implementation," *IEEE Trans. Veh. Technol.*, vol. 67, no. 10, pp. 9129–9144, 2018.
- [52] D. He, B. Ai, K. Guan, Z. Zhong, B. Hui, J. Kim, H. Chung, and I. Kim, "Channel measurement, simulation, and analysis for high-speed railway communications in 5G millimeter-wave band," *IEEE Trans. Intelligent Transportation Sys.*, vol. 19, no. 10, pp. 3144–3158, 2018.
- [53] 3GPP TR 36.878 (V13.0.0), "Study on performance enhancements or high speed scenario in LTE," 2016.
- [54] J. Zhang, T. Chen, S. Zhong, J. Wang, W. Zhang, X. Zuo, R. G. Maunder, and L. Hanzo, "Aeronautical Ad Hoc networking for the internet-above-the-clouds," *Proc. IEEE*, vol. 107, no. 5, pp. 868–911, 2019.
- [55] EUROCONTROL, "Updated LDACS1 system specification," [Online]. Available: <http://www.ldacs.com/wp-content/uploads/2014/02/LDACS1-Updated-Specification-Proposal-D2-Deliverable.pdf>.
- [56] E. Haas, "Aeronautical channel modeling," *IEEE Trans. Veh. Technol.*, vol. 51, pp. 254–264, Mar 2002.
- [57] R. Sun, D. W. Matolak, and W. Rayess, "Air-ground channel characterization for unmanned aircraft systems – Part IV: Airframe shadowing," *IEEE Trans. Veh. Technol.*, vol. 66, pp. 7643–7652, Sept 2017.
- [58] 3GPP Technical Report 21.915, "Summary of Rel-15 work items," [Online]. Available: <http://www.3gpp.org/release-15>.
- [59] L. Hanzo, O. Alamri, M. El-Hajjar, and N. Wu, *Near-Capacity Multi-Functional MIMO Systems: Sphere-Packing, Iterative Detection and Cooperation*. John Wiley & Sons, May 2009.
- [60] S. X. Ng and L. Hanzo, "On the MIMO channel capacity of multidimensional signal sets," *IEEE Trans. Veh. Technol.*, vol. 55, no. 2, pp. 528–536, 2006.
- [61] C. Xu, S. Sugiura, S. X. Ng, P. Zhang, L. Wang, and L. Hanzo, "Two decades of MIMO design tradeoffs and reduced-complexity MIMO detection in near-capacity systems," *IEEE Access*, vol. 5, pp. 18564–18632, 2017.
- [62] R. E. Fischer, L. H. Lampe, and S. Calabro, "Differential encoding strategies for transmission over fading channels," *Int. J. Electron. Commun.*, vol. 54, no. 1, pp. 59–67, 2000.
- [63] L. H. Lampe and R. Schober, "Low-complexity iterative demodulation for noncoherent coded transmission over Ricean-fading channels," *IEEE Trans. Veh. Technol.*, vol. 50, no. 6, pp. 1481–1496, 2001.
- [64] C. Xu, S. X. Ng, and L. Hanzo, "Multiple-symbol differential sphere detection and decision-feedback differential detection conceived for differential QAM," *IEEE Trans. Veh. Technol.*, vol. 65, no. 10, pp. 8345–8360, 2016.
- [65] C. Xu, L. Wang, S. X. Ng, and L. Hanzo, "Soft-decision multiple-symbol differential sphere detection and decision-feedback differential detection for differential QAM dispending with channel estimation in the face of rapidly fading channels," *IEEE Trans. Wireless Commun.*, vol. 15, no. 6, pp. 4408–4425, 2016.
- [66] R. Schober, W. H. Gerstacker, and J. B. Huber, "Decision-feedback differential detection of MDPSK for flat Rayleigh fading channels," *IEEE Trans. Commun.*, vol. 47, no. 7, pp. 1025–1035, 1999.
- [67] R. Schober and W. H. Gerstacker, "Decision-feedback differential detection based on linear prediction for MDPSK signals transmitted over Ricean fading channels," *IEEE Journal on Selected Areas in Commun.*, vol. 18, pp. 391–402, Mar. 2000.
- [68] R. Schober, W. H. Gerstacker, and J. B. Huber, "Decision-feedback differential detection based on linear prediction for 16DPSK signals transmitted over flat Ricean fading channels," *IEEE Trans. Commun.*, vol. 49, pp. 1339–1342, 2001.
- [69] V. Tarokh and H. Jafarkhani, "A differential detection scheme for transmit diversity," *IEEE J. Sel. Areas Commun.*, vol. 18, no. 7, pp. 1169–1174, 2000.
- [70] G. Ganesan and P. Stoica, "Differential modulation using space-time block codes," *IEEE Signal Process. Lett.*, vol. 9, no. 2, pp. 57–60, 2002.
- [71] R. Schober and L. H. Lampe, "Noncoherent receivers for differential space-time modulation," *IEEE Trans. Commun.*, vol. 50, no. 5, pp. 768–777, 2002.
- [72] X. Xia, "Differentially en/decoded orthogonal space-time block codes with APSK signals," *IEEE Commun. Lett.*, vol. 6, no. 4, pp. 150–152, 2002.
- [73] C. Xu, L. Wang, S. X. Ng, and L. Hanzo, "Multiple-symbol differential sphere detection aided differential space-time block codes using QAM constellations," *IEEE Signal Process. Lett.*, vol. 18, no. 9, pp. 497–500, 2011.
- [74] C. Hwang, S. H. Nam, J. Chung, and V. Tarokh, "Differential space time block codes using nonconstant modulus constellations," *IEEE Trans. Signal Process.*, vol. 51, no. 11, pp. 2955–2964, 2003.
- [75] W. Yuan, S. Li, Z. Wei, J. Yuan, and D. Ng, "Data-aided channel estimation for OTFS systems with a superimposed pilot and data transmission scheme," *IEEE Wireless Commun. Letts.*, vol. 10, no. 9, pp. 1954–1958, 2021.
- [76] A. Baptista, "ACARS - aircraft communication and reporting system," [Online]. Available: <https://www.scribd.com/document/337194948/ACARS-Aircraft-Communication-Adressing-and-Reporting-System>.
- [77] EUROCONTROL, "ADS-B for dummies," [Online]. Available: [https://www.sigidwiki.com/images/1/15/ADS-B\\_for\\_Dummies.pdf](https://www.sigidwiki.com/images/1/15/ADS-B_for_Dummies.pdf).
- [78] J. C. Belfiore, G. Rekaya, and E. Viterbo, "The Golden code: a 2x2 full-rate space-time code with nonvanishing determinants," *IEEE Trans. Inf. Theory*, vol. 51, pp. 1432–1436, April 2005.
- [79] F. Oggier, G. Rekaya, J. C. Belfiore, and E. Viterbo, "Perfect space-time block codes," *IEEE Trans. Inf. Theory*, vol. 52, pp. 3885–3902, Sept 2006.
- [80] K. P. Srinath and B. S. Rajan, "Improved perfect space-time block codes," *IEEE Trans. Inf. Theory*, vol. 59, pp. 7927–7935, Dec 2013.
- [81] R. W. Heath and A. J. Paulraj, "Linear dispersion codes for MIMO systems based on frame theory," *IEEE Trans. Signal Process.*, vol. 50, pp. 2429–2441, Oct 2002.
- [82] B. Hassibi and B. M. Hochwald, "Cayley differential unitary space-time codes," *IEEE Trans. Inf. Theory*, vol. 48, no. 6, pp. 1485–1503, 2002.
- [83] C. Xu, S. Sugiura, S. X. Ng, and L. Hanzo, "Spatial modulation and space-time shift keying: Optimal performance at a reduced detection complexity," *IEEE Trans. Commun.*, vol. 61, pp. 206–216, January 2013.
- [84] S. Sugiura, S. Chen, and L. Hanzo, "Coherent and differential space-time shift keying: A dispersion matrix approach," *IEEE Trans. Commun.*, vol. 58, pp. 3219–3230, November 2010.
- [85] S. Sugiura, T. Ishihara, and M. Nakao, "State-of-the-art design of index modulation in the space, time, and frequency domains: Benefits and fundamental limitations," *IEEE Access*, vol. 5, pp. 21774–21790, 2017.
- [86] C. Xu, P. Zhang, R. Rajashekar, N. Ishikawa, S. Sugiura, Z. Wang, and L. Hanzo, "Near-perfect finite-cardinality generalized space-time shift keying," *IEEE J. Sel. Areas Commun.*, vol. 37, no. 9, pp. 2146–2164, 2019.
- [87] C. Xu, T. Bai, J. Zhang, R. G. Maunder, S. Sugiura, Z. Wang, and L. Hanzo, "Constant-envelope space-time shift keying," *IEEE J. Sel. Topics Signal Process.*, vol. 13, no. 6, pp. 1387–1402, 2019.



**Chao Xu** (S'09-M'14-SM'19) is currently a senior lecturer at University of Southampton, UK. His research interests include index modulation, reconfigurable intelligent surfaces, optical wireless and quantum communications. In 2023, he was awarded Marie Skłodowska-Curie Actions (MSCA) Global Postdoctoral Fellowships with the highest evaluation score of 100/100.



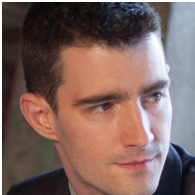
**Luping Xiang** received the B.Eng. degree (Hons.) from Xiamen University, China, in 2015, and the Ph.D. degree from the University of Southampton, in 2020. From 2020 to 2021 He was a Research Fellow with the Next Generation Wireless Group, University of Southampton. He began a lectureship in November 2021 at School of Information and Communication Engineering, University of Electronic Science and Technology of China. His research interests include machine learning, channel coding and modulation/demodulation.



**Geoffrey Ye Li** is currently a Chair Professor at Imperial College London, UK. Before joining Imperial in 2020, he was a Professor at Georgia Institute of Technology, USA, for 20 years and a Principal Technical Staff Member with AT&T Labs Research (previous Bell Labs) in New Jersey, USA, for five years. He won 2024 IEEE Eric E. Sumner Award and several awards from IEEE Signal Processing, Vehicular Technology, and Communications Societies, including 2019 IEEE ComSoc Edwin Howard Armstrong Achievement Award.



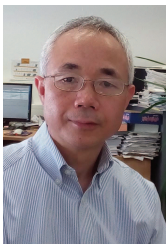
**Shinya Sugiura** (M'06–SM'12) received the Ph.D. degree in electronics and electrical engineering from the University of Southampton, Southampton, U.K., in 2010. He is an Associate Professor with the Institute of Industrial Science, The University of Tokyo, Tokyo, Japan. He authored or coauthored over 100 IEEE journal papers. University of Southampton, Southampton, U.K., in 2010.



**Prof Robert G. Maunder** began a lectureship in November 2007 and was promoted to Associate Professor in March 2013 and to Professor in August 2017. His research interests include joint source/channel coding and the holistic design of algorithms and hardware implementations for wireless communications. He is the founder and CTO of AccelerComm Ltd, which is commercialising his research as soft-IP.



**Robert Schober** is an Alexander von Humboldt Professor and the Chair for Digital Communication at Friedrich-Alexander University of Erlangen-Nuremberg, Germany. His research interests fall into the broad areas of Communication Theory, Wireless and Molecular Communications, and Statistical Signal Processing.



**Lie-Liang Yang** (M'98, SM'02, F'16) is the professor of wireless communications at the University of Southampton. He has research interest in wireless communications, wireless networks, and signal processing for wireless communications as well as molecular communications and nanonetworks. He is a Fellow of IET and AAIA. Further details at: <https://www.ecs.soton.ac.uk/people/llyang>.



**Lajos Hanzo** (FIEEE'04) received Honorary Doctorates from the Technical University of Budapest (2009) and Edinburgh University (2015). He is a Foreign Member of the Hungarian Science-Academy, Fellow of the Royal Academy of Engineering (FREng), of the IET, of EURASIP and holds the IEEE Eric Sumner Technical Field Award. For further details please see <http://www-mobile.ecs.soton.ac.uk>, [https://en.wikipedia.org/wiki/Lajos\\_Hanzo](https://en.wikipedia.org/wiki/Lajos_Hanzo).



**Dusit Niyato** (M'09-SM'15-F'17) is a professor in the School of Computer Science and Engineering, at Nanyang Technological University, Singapore. He received B.Eng. from King Mongkuts Institute of Technology Ladkrabang (KMITL), Thailand in 1999 and Ph.D. in Electrical and Computer Engineering from the University of Manitoba, Canada in 2008. His research interests are in the areas of sustainability, edge intelligence, decentralized machine learning, and incentive mechanism design.